Refining the Spectroscopic Techniques for the Characterization of Single Molecule Magnets

Submitted to the Department of Physics of Amherst College
in partial fulfillment of the requirements for the degree of
Bachelor of Arts with Honors

May 2014

by

Andrew Mowry

advised by

Prof. Jonathan Friedman

Amherst College
Dept. of Physics

Abstract

Single molecule magnets, a class of paramagnetic molecules that can be approximated in their bulk form as an ensemble of weakly interacting large spins, show much promise for applications in quantum computing and also for basic physics research. Advancement in these areas depends on the characterization of SMMs, with which the Friedman Laboratory has been engaged for many years. This thesis investigates the inefficiencies of the apparatus and procedures previously used for characterization of SMMs using electron spin resonance techniques, and details the improvements made to each, most consequentially in the spectral measurement process and the functionality of the apparatus at high magnetic fields. Specifically, the design of a probe assembly that allows *in situ* rotation of the sample-resonator system improves the experiment's performance in high fields; and the acquisition of complex transmission data and the automation of data collection and processing enable characterizations to proceed more quickly and more precisely than before. Hopefully these improvements will aid in the future study of single molecule magnets.

Acknowledgments

To Yiming Chen I owe many more thanks than can responsibly be added to the body of this text. I am ever grateful for the consistent work that he contributed to this project, for the friendly company that he provided in the lab, and for the interesting conversations we had. I wish him all the best.

Jim Kubasek truly deserves his reputation at Amherst College and then some more. Always eager to give the hand he knows we all need, he is a pleasure to work with. I thank him for all the work that he so gladly did to help turn the idea of the PPMS probe into a reality.

Paul Chapin should also be thanked for generously donating his time, patience, and 3d printer to my endless circuit board holder iterations. I tried to write "please" and "thank you" in every new request I sent to him, but by the tenth time it no longer felt like enough. Thanks Paul.

Changyun Yoo, despite his increasingly frequent absences from the lab during the second semester, still warrants my thanks for the company he did give, which made my lab experiences much more enjoyable. I hope he enjoys his own thesis research next year.

Last but certainly not least, I thank Professor Jonathan Friedman for his relentless support over the year. From our first Skype meeting before the summer to the furious days before this document was submitted, he has been nothing but helpful and patient with my repeated questions. For his guidance and for his welcoming me into his lab I am grateful.

Funding and support for this research is due to the National Science Foundation under grants DMR-1006519 and DMR-1310135, and also to the Amherst College Dean of Students.

Contents

List of Figures

Chapter 1

Introduction

Single molecule magnets (SMMs) as a class of molecules have featured in several exciting research projects over the past few decades, and electron spin resonance (ESR) as a technique to characterize their properties has been steadily popular. The interest in SMMs throughout the physics and chemistry communities is due largely to their unique position straddling the quantum-classical divide, and the applications that this implies. On the one hand, SMMs have macroscopic magnetic properties that can be interacted with and measured through classical methods; on the other hand, the unique structural composition of SMMs causes samples to exhibit quantum behaviors that are normally associated with physics on the microscopic scale.

Perhaps the most exciting of the applications proposed for single molecule magnets is their integration into quantum computers as qubits. In this capacity SMMs are competing with other technologies, like quantum dots, superconducting circuits, and impurities in diamonds. Given the present vigor of research into quantum information processing, each of these technologies has a strong body of foundational research, and the relative strengths and weaknesses of each is becoming clearer.[1] Macroscopic superconducting circuits, for example, are obviously addressable, while preliminary research suggests that the magnetic relaxation times of SMMs, the scale of which is vital for quantum memory storage, can be superior to other technologies [30]. The most realistic roles for SMMs in quantum computing, then, would be in so-called hybrid systems, which propose to integrate the strengths and weaknesses of various quantum devices into a single system [23]. Much research is currently being invested into pushing the coherence times of SMMs even further to capitalize on this relative strength.[2]

Independent of the particular outcome of the quantum computer engineering race, the uses of SMMs for the pursuit of basic physics research seem numerous. They have provided, for example,

[1] For a review of research into physical systems that might support quantum computing, see Ladd [16].
[2] For a discussion specifically on the feasibility of SMMs in quantum computers, see Ardavan [3].

the observation of macroscopic spin tunneling [10] and Berry phase interference [28], and also provided further insight into the feasibility of some quantum mechanical models, like the Giant Spin Approximation [29].

This thesis does not report new physics on SMMs, but instead presents some advances in the techniques surrounding their study, specifically their study by methods of ESR. Many of the improvements made will necessarily be limited in scope to future investigations in Professor Friedman's Laboratory, but in particular the development of a device for *in situ* rotation of superconducting resonators may have broader applicability. Hopefully the work that this thesis represents will allow for future progress in the field of SMM research.

The Properties of Single Molecule Magnets[3]

The class of compounds known as single molecule magnets has come to be restricted to those with a few characteristic qualities, which we sketch. A sample of SMMs is a crystal lattice of molecules, each of which consists of a magnetic core and a large, surrounding ligand structure. The magnetic core is composed of paramagnetic transition metal ions, each of which hosts at least one unpaired electron. The diamagnetic ligand structure of the SMM surrounds the magnetic core and importantly serves as a buffer between neighboring cores: repulsive ligand-ligand interactions between individual molecules prevent an overly dense crystal lattice from forming, and so the intermolecular forces acting between single SMMs are small enough to be neglected. As an example, a drawing of a Mn_{12} SMM[4] is shown in Fig. 1.1, wherein the core and ligand structures are easily visible.

Modeling the behavior of an SMM by describing its energetics is a daunting prospect. There are a host of interactions to take into account — spin-spin, spin-orbit, spin-lattice, Zeeman, etc. — so that any practical attempt at description requires several assumptions to be made. Under the Giant Spin Approximation (GSA),[5] which we use for our research, the magnetic core of many spins can be simplified into one effective spin, and ligand interactions are simplified into an overall crystal lattice potential. In this way modeling the behavior of the molecule becomes tractable.

Taken together, the GSA and the effects of the ligand structures allow us to approximate a sample of crystalline SMMs as an ensemble of large, isolated spins, and this is of experimental interest precisely for the reason given above: the ability to observe both traditionally macroscopic and traditionally microscopic effects together. Advances in synthetic chemistry fabrication techniques

[3] Information from this section is informed primarily by Abragam [1] and Lawrence [17].
[4] $Mn_{12}O_{12}(O_2CC_4H_3S)_{16}(H_2O)_4$
[5] See Appendix B for an elaboration on the Giant Spin Approximation.

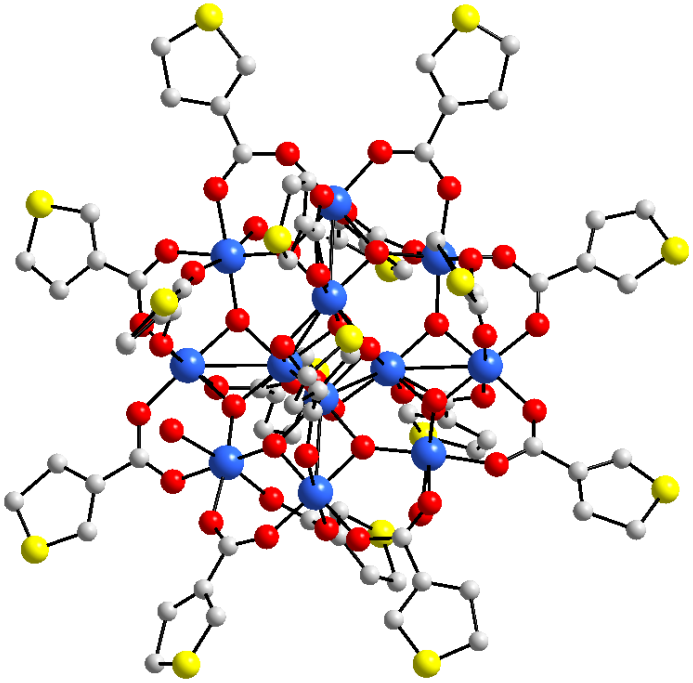

Figure 1.1: Drawing of the Mn_{12} SMM [19]. The magnetic core of Mn ions is colored blue, and the surrounding ligand structure is easily visible.

now permit crystals to be grown to sizes exceeding 10^{15} spins [14]; such large ensembles imply that the samples may develop strong net magnetizations and so allow for macroscopic interactions.

The Hamiltonians published in the literature to describe SMMs predominantly take the form

$$\hat{H} = -D\hat{S}_z^2 - (\text{additional anisotropy terms}) - g\mu_B B\hat{S}_n, \tag{1.1}$$

and are thus distinguished by an axially anisotropic term (the z-axis is chosen to coincide with such an axis, hereafter termed the "easy axis"), an assortment of additional anisotropic terms that reflect structural symmetries of the molecule (usually determined by the ligands), and the Zeeman interaction term, where $\hat{S}_n$ is the projection of the spin operator in the direction of the external magnetic field B. For further information on the source of these terms and their determinations, the reader is referred to Appendix B.

The Zeeman term is well known, and breaks the energy eigenvalue degeneracy with a linear dependence on external magnetic field strength.

Introducing the $-D\hat{S}_z^2$ term leads to more interesting behavior, though, creating a preferred axis for magnetization along the easy-axis of the molecule: eigenstates with larger $|m_s|$ values are energetically preferred. Since the $\hat{S}_z$ operator is squared, the $\pm m_s$ energy eigenstates are degenerate,

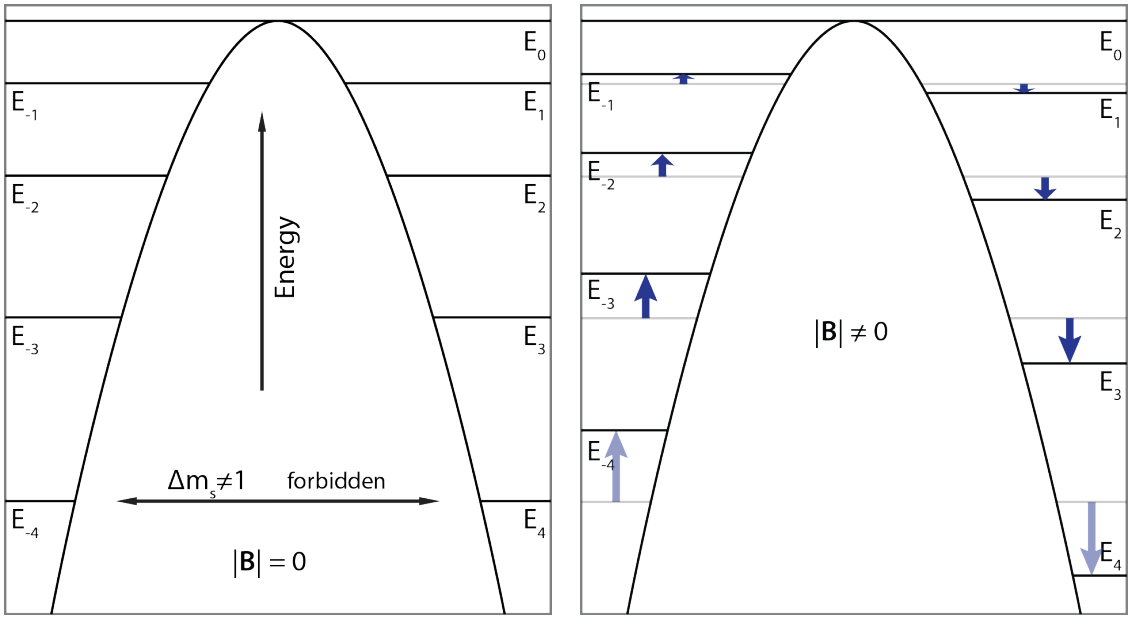

Figure 1.2: Double well potential without (a) and with (b) the Zeeman interaction, which skews the eigenvalues on either side of the potential barrier at non-zero magnetic fields.

and so there is not a preferred *direction* for magnetization at zero-field. Indeed, by the quantum selection rule that $\Delta m_s = \pm 1$ a large energy barrier exists that hinders magnetization reversal along the easy axis; tunneling between the ground states — the two, opposite sign, lowest energy states — is prohibited. If we visualize the barrier as an inverse parabola, as in Fig. 1.2, we see how one of the degenerate ground states must "climb over" the potential to get to the other ground state. Now considering the $-D\hat{S}_z^2$ term in conjunction with the Zeeman term, the energy barrier is maintained and a single magnetization direction becomes preferred along the easy-axis at non-zero magnetic fields. Referring again to Fig. 1.2, the energy levels on opposite sides of the barrier shift relative to one another to reflect the different energetics, and the ground state degeneracy is broken.

The effect of adding off-diagonal[6] anisotropic terms to the Hamiltonian, such as $E(\hat{S}_x^2 - \hat{S}_y^2)$, is to create new eigenstates that are superpositions of the old ones. For most values of the magnetic field these superpositions are dominated by just one state, and so the field-dependent behavior is similar to that above, without the off-diagonal terms. At small fields, though, and near where two eigenvalues might become degenerate (as in Fig. 1.3), there can be significant mixing of states so as to create "avoided level crossings" or "tunnel splittings". At the middle of the tunnel splittings the states mix with equal magnitudes: $|\Psi\rangle = \left(1/\sqrt{2}\right)|m_s = -1\rangle \pm \left(1/\sqrt{2}\right)|m_s = 2\rangle$, for example. [1]

[6]Off-diagonal terms in the Hamiltonian can also be created by moving the magnetic bias field out of alignment with the z-axis.

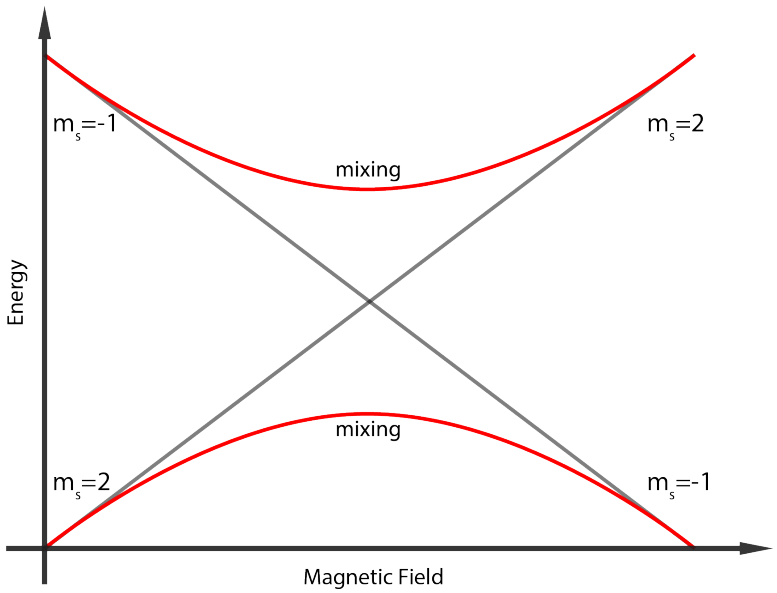

Figure 1.3: Avoided level crossing. The gray lines indicate the expected behavior of unmixed eigenstates due only to the Zeeman interaction, while the red lines show the actual behavior of mixed eigenstates due to anisotropic energy terms and/or an off-z-axis magnetic bias field.

Tunnel splitting can be understood as a phenomenon surrounding stationary points in the Hamiltonian's parameter space (the parameter in this case being the magnetic field), and one is sometimes referred to as a "sweet spot". The "sweet spot" is of significance because given a small change in the parameters of the Hamiltonian, the energy eigensystem is negligibly impacted. Practically, an SMM operated in this regime will be only minimally affected by noise fluctuations in the parameter space, and so information loss due to decoherence is minimized. The reader is referred to Adams' thesis for more information [2].

To provide more intuition for the above discussion on the terms of Eq. 1.1, we present a graphical summary of the energy eigenvalues in Fig. 1.4. The frames of the figure consecutively add the Zeeman, axial anisotropic, and off-axial anisotropic terms to a conjectured spin-1 system. In the final frame we see the low field behavior — broken degeneracy and tunnel splitting — and the high field behavior — approximately unmixed Zeeman splitting.

Electron Spin Resonance[7]

We characterize SMMs in ESR by measuring the power absorption of energy transitions. Given a system like that in Fig. 1.4c, we see that there are three possible transitions: accurately enough represented in the strong field as $|+1\rangle \Leftrightarrow |0\rangle$, $|-1\rangle \Leftrightarrow |0\rangle$, and $|+1\rangle \Leftrightarrow |-1\rangle$ (the latter is only

[7]Information from this section is informed by Abragam [1] and Lawrence [17].

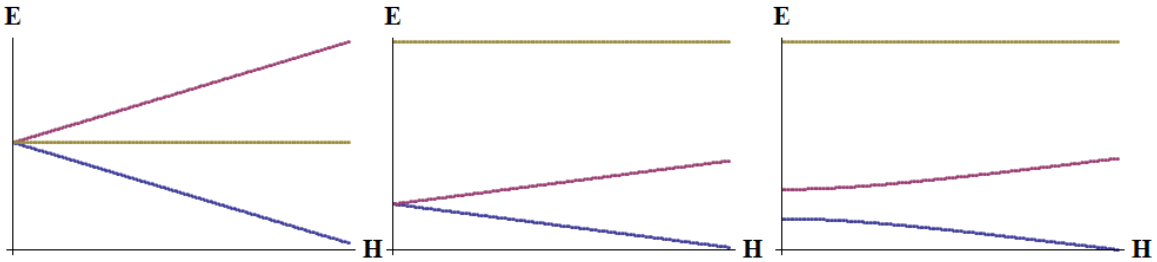

(a) (b) (c)

Figure 1.4: Effects of the SMM Hamiltonian terms on energy eigenvalues against a magnetic field applied along the z-axis. (a) corresponds to $\hat{H} = -g\mu_B B\hat{S}_n$, (b) corresponds to $\hat{H} = -D\hat{S}_z^2 - g\mu_B B\hat{S}_n$, and (c) corresponds to $\hat{H} = -D\hat{S}_z^2 - (\text{additional anisotropy terms}) - g\mu_B B\hat{S}_n$.

weakly allowed).[8] The energy transitions are quantized by $\Delta E = \hbar\omega$, which, due to the Zeeman interaction, is a field dependent quantity. If we provide this energy by applying an oscillating RF field, then we can drive spins in the low energy state to the high energy state.

We temporarily restrict ourselves to the $|+1\rangle \Leftrightarrow |-1\rangle$ transition from Fig. 1.4c, and consider the whole system as just two states: an excited and a ground state. (This is not an awful assumption if we constrain ourselves to the low-field regime where $\Delta E_{|+1\rangle\Leftrightarrow|-1\rangle} \ll \Delta E_{|\pm1\rangle\Leftrightarrow|0\rangle}$.) Applying Boltzmann statistics to the ensemble of (approximately) non-interacting spins, we see that the equilibrium population of spins in the state $|+1\rangle$ relative to that in the state $|-1\rangle$

$$\frac{n_{|+1\rangle}}{n_{|-1\rangle}} = \exp\left(-\frac{E_{|+1\rangle} - E_{|-1\rangle}}{kT}\right) \tag{1.2}$$

is less than unity since $\Delta E = \left(E_{|+1\rangle} - E_{|-1\rangle}\right)$ is positive. So power is (on average) absorbed by the sample of SMMs at resonance, and because of the great number of spins contained in the sample the power will be macroscopic, even for population ratios close to one. As an example, we look at a 5 GHz transition at 1.8 K; these values are roughly the conditions that we investigate during our ESR studies. It follows directly from Eq. 1.2 that $(n_{|+1\rangle}/n_{|-1\rangle}) \approx .875$, and so there are significantly fewer spins in the excited state at thermodynamic equilibrium than are in the ground state, resulting in a net absorption of energy upon application of 5 GHz radiation. Eq. 1.2 also shows one advantage of working at very low temperatures: a low temperature increases the population of the ground state relative to that of the excited state so that the absorbed power is greater. This serves to increase the effective sensitivity of ESR measurements.

The net absorption of energy that we calculated does not necessarily imply a steady power absorption: the sample must maintain a positive population bias in the ground state for continuous

[8] In the weak field, the eigenstates are significantly mixed, as noted above, and so the $|+1\rangle \Leftrightarrow |-1\rangle$ transition becomes more significant. (At least heuristically; labelling the states as such at weak field is inaccurate.)

absorption, and so there must be spin relaxation concurrent with the spin excitation. There are two mechanisms for spin relaxation: spin-lattice relaxation, characterized by T_1, and spin-spin relaxation, characterized by T_2. Spin-lattice relaxation is the loss of energy to the surrounding crystal lattice via thermal processes, and spin-spin relaxation is the dephasing of spins relative to one another.[9] We see that if the spins do not relax quickly enough, the sample will saturate under continuous excitement and the absorbed power will quickly become negligible.[10]

Experimental determination of the total relaxation rate $\Gamma = \frac{1}{T_1} + \frac{1}{T_2}$ requires careful measurements of a sample's net magnetization (to determine population ratios) and absorbed power (to determine rates) and then to equate terms such that a steady state is achieved. Such a determination for Ni_4, one of the SMMs we attempted to measure during this research, has been conducted by de Loubens [7] and shows a negative correlation between relaxation rates and temperature (high temperatures have low relaxation rates). Thus we have a second reason to operate ESR at low temperatures: we are less likely to saturate the sample.

The approach we take to measuring power absorption in this thesis is to mount a sample of SMMs onto a superconducting coplanar waveguide resonator, characterized by its own resonant modes.[11] The combined system of the resonator and one spin is described by the Jaynes-Cummings Hamiltonian

$$\hat{H} = \hat{H}_{\text{res}} + \hat{H}_{\text{spin}} - \overrightarrow{\mu} \cdot \overrightarrow{B}, \tag{1.3}$$

where the individual Hamiltonians for the resonator and spin add together with an additional interaction term: $\overrightarrow{B}$ is the magnetic field generated by the oscillating current in the resonator, and $\overrightarrow{\mu}$ is the magnetic dipole of an SMM's spin [14].

The dynamics of this combined system are describable by the strength of the interaction term, which is proportional to a coupling constant, g. In the weak-coupling regime $g \ll \delta$, where δ is a characteristic damping measure; and so the spin-resonator interaction is negligible. The eigenvalues of the Hamiltonian are dominated by those of the uncoupled resonator, and the system behaves much as does the bare resonator.

In the case of strong coupling, where $g \gg \delta$, the spin-resonator interaction becomes coherent and the eigenvalues of the system change [4]. Strong coupling occurs when $E_{|+1\rangle} - E_{|-1\rangle} \approx \hbar\omega_{\text{res}}$ (i.e.

[9] T_1 and T_2 are very interesting quantities for researchers studying the hardware of quantum computing. Since information can only be stored in a qubit so long as its state is known, the characteristic relaxation times for a substance measure the duration it can remain in a known state, on average. In particular, T_2 is of interest.

[10] The issue of saturation has sometimes bothered us in our research. See Chapter 5 Section 5.

[11] See Appendix D Section for details on the resonator we use.

where the sample's energy of transition is close to the resonator's energy of resonance) and when the interaction term is sufficiently strong. Although the strength of a single spin-resonator interaction might be on the order of only 100 Hz, the strength of a combined *ensemble*-resonator interaction is multiplied by a factor of $\sqrt{N}$, where N is the number of spins interacting with $\overrightarrow{B}$, the magnetic field produced by the RF signal in the resonator [14].[12] Some SMM samples have thus been calculated to have coupling energies as high as 2-3 GHz [14].[13]

Stealing a glance ahead at Fig. 2.7, we can see that even a deviation from the bare resonator's energetics on the order of 1 MHz is not too small to be noticed for the typical experiment we run. If a deviation would occur during an experiment, we could infer the energy of the spin transition $\Delta E_{|+1\rangle \Leftrightarrow |-1\rangle}$ by its location, and so for sufficient powers and sample sizes, the above described approach to ESR should provide a dependable way of characterizing an SMM's energetics.

Forthcoming Chapters

The remainder of this thesis will discuss, in a loosely narrative format, the design and development of an apparatus to efficiently carry out electron spin resonance experiments. Asides to discuss motivational or supporting physical theory are placed appropriately, although they are relegated to the Appendices where possible so as not to breakup the flow of the narrative. Since this thesis was begun as a results-oriented project, we present collected data near the conclusion even though it shows the lack of the expected observations; the data serves more usefully as a characterization of the apparatus that is portrayed beforehand.

[12] There are many assumptions and omissions in presenting this constant, so it should be taken heuristically.
[13] This coupling energy was calculated for a transmission in Tb_{30}.

Chapter 2

Apparatus and Procedure[1]

Since Adams' research methods and experimental setup matched closely with ours at the beginning of the research — indeed, this thesis was explicitly begun as a continuation of his work — we were able to begin right away with experimentation. Where a new experiment would have necessitated thought on experimental design at the beginning, we were able to take an iterative approach to multiple experimental redesigns. We will thus begin the chapter by detailing the three broad "generations" that our experimental apparatus evolved through over the course of the year, starting with a description of Adams' design. The early exposition of the apparatus will make subsequent discussions much more convenient.

Broadly Speaking

The purpose of our apparatus, broadly speaking, is to record the transformations that a particular circuit imparts on a passing electrical signal. More specifically, we mount an SMM sample on a superconducting resonator and pass a signal through it, expecting frequency dependent transformations: we thus record the output signal from the circuit over a range of frequencies to analyze this behavior. By purpose, then, all of the apparatuses we present are of the same general design, since they are all used to capture the same raw data, and they can be reduced to the following three steps (shown in Fig. 2.1):

1. A high frequency signal is generated;

[1] We in the present research had the great advantage of beginning with many procedures and pieces of equipment in place; Spencer Adams, the previous thesis writer in the Friedman Lab, conducted electron spin resonance (ESR) experiments on single molecule magnets (SMMs) in ways very similar to how we conducted them, and we benefit from his work.

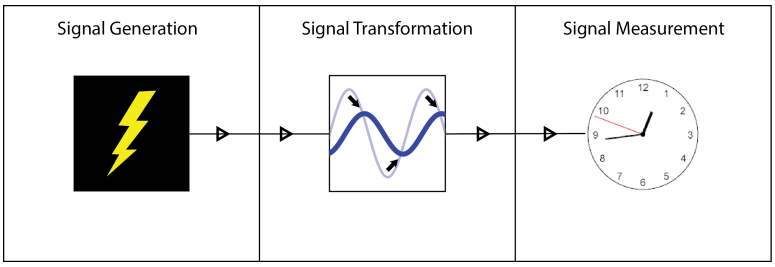

Figure 2.1: General apparatus schematic. The three stages of all of the apparatuses we present here: signal generation, signal transformation, and signal measurement.

2. The signal is routed through the resonator, where it undergoes some transformation;

3. The output signal, modified by the resonator, is measured.

The generality of this outline invites imagination of the different permutations it might take. How should the signal be generated? What should the signal look like? How should it be measured? Under what conditions should we keep the resonator? The bulk of this chapter will discuss these questions, offering our solutions and justifications for those design choices.

There are some conditions that we took as constant during the process of optimization: most notably, the part of the apparatus responsible for maintaining our resonators under predictable conditions. The resonators we used — niobium coplanar waveguide resonators — need to be operated below around 9.2 K, which is their critical temperature. (Niobium is a Type II superconductor.) Furthermore, their resonant properties are very sensitive to small changes in temperature below that threshold and also to stray magnetic fields; mechanical vibrations that would subtly alter the electrical connections between the resonator and the rest of the circuit would also be troublesome. Because of these considerations, a robust piece of equipment capable of isolating the resonator at low, measurable, and manipulable temperatures and magnetic fields is necessary. The Physical Property Measurement System (PPMS), sold by Quantum Design, is this robust piece of equipment. It conveniently provides the integrated environmental conditioning required by our experiment.

Physically, the PPMS is a large, nitrogen-jacketed dewar of liquid helium with a probe cavity/sample space that accommodates a long probe for experimental use. (We sketch the geometry of the PPMS in Fig. 2.2 and a more detailed view of the probe cavity in Fig. 2.3 for context.) At the very base of the probe cavity is the "control zone" of the PPMS, which is the area in which the precise thermal and magnetic conditions are known and manipulable through a physical user interface. The temperature is controlled via two "impedances" that regulate interaction between

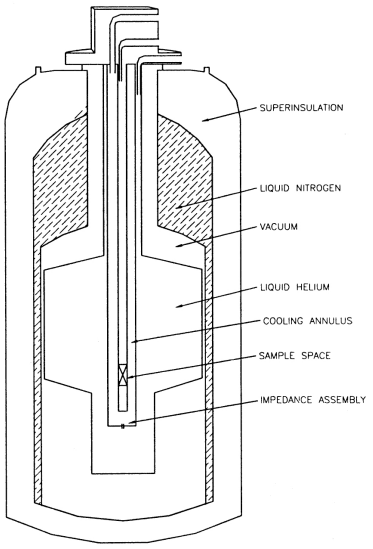

Figure 2.2: Schematic of the PPMS dewar, with copyrights to Quantum Design. The probe is inserted through the top of the probe cavity/sample space such that its end, which holds the resonator, rests inside the control zone, marked with an x in the figure. Reproduced with permission from the PPMS hardware manual.

the helium and the probe cavity;[2] the magnetic field is set using a current driver and a superconducting solenoid that surrounds the probe cavity. The probe holds the experiment — in our case the resonator — inside the control zone and connects it through a hermetic seal via cabling to the exterior of the PPMS.

Using the PPMS does constrain our design, but not overwhelmingly so, and mostly in terms of the geometry of the probe. For the purposes of this chapter on the apparatus and procedure we withhold discussion of the probe design, even though it forms a major part of the advances in the experimental design. We will instead evaluate the probe in Chapter 4, after first having developed some superconductivity theory that motivates the design choices.

The following pages will contain descriptions of the three generations of apparatus that we worked with throughout the year. Each generation builds on the last, and each offers significant improvements over the last such that there is normally no need to revisit past designs. In defining "improvements" it is useful to condense the function of the apparatus into two measures: speed and precision of data acquisition,[3] and types of data able to be acquired. Although we no longer use the first generation apparatus, we present it as a means of gaining familiarity with its components, which

[2]The impedances are small coils that permit helium to enter the cooling annulus from the reservoir. The default state is for freely flowing helium, but this flow can be blocked with a small bubble by heating the impedances: fresh helium would thus be prevented from entering the annulus.

[3]The speed and precision of measurement constitute one quality since the two are related quantities: for any given apparatus the precision may be improved by reducing the speed, and vice versa.

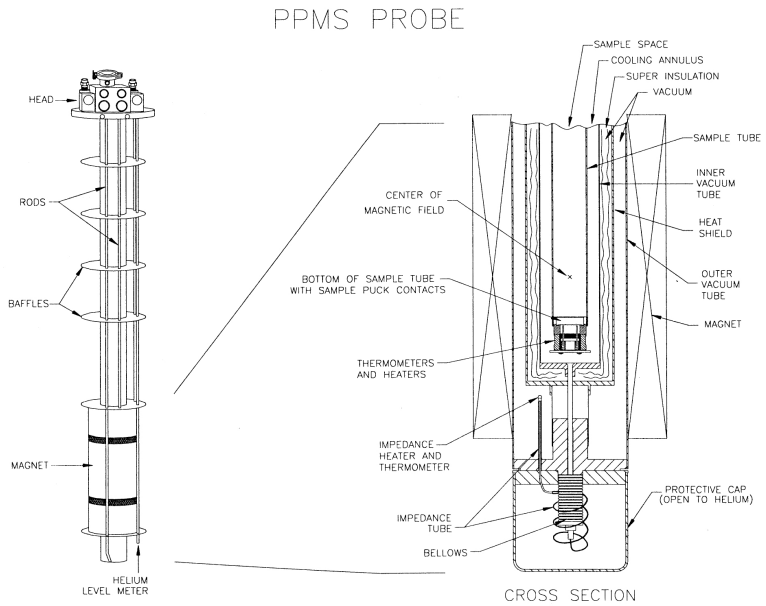

Figure 2.3: Schematic of the PPMS probe assembly, with copyrights to Quantum Design. The probe assembly contains magnetic coils, the impedance heater, and also the hollow for the probe cavity/sample space. Reproduced with permission from the PPMS hardware manual.

are reused, and as a means of gaining some context on the experiment. The second generation is an incremental but unimaginative improvement on the first, which nevertheless needs to be explained since it is sometimes used when the third generation, sometimes buggy, is not functioning properly. It should be understood that the third generation, though, stands as the most capable apparatus. Each apparatus has more than one "permutation," or mode of configuration, such that it can take data at various speeds and precision.

First Generation (1G)

The 1G apparatus was inherited from Adams as a working whole, and has two permutations: the first (1P), shown in Fig. 2.4 (a), takes data quickly but imprecisely; the second (2P), Fig. 2.4 (b), is used for more precise data acquisition but takes relatively more time. The permutations take nearly the same form, and differ only in the means of measurement: a signal is produced by an RF generator, passes through a stack of RF attenuators, routes into the PPMS and through the resonator, is converted to a DC signal by a power diode, and is then measured. The 1P apparatus uses an oscilloscope for measurement, while the 2P apparatus measures the signal automatically with a LabView routine controlling a digital multimeter.

The 1P apparatus is designed for diagnostic viewing, not data acquisition; the oscilloscope's

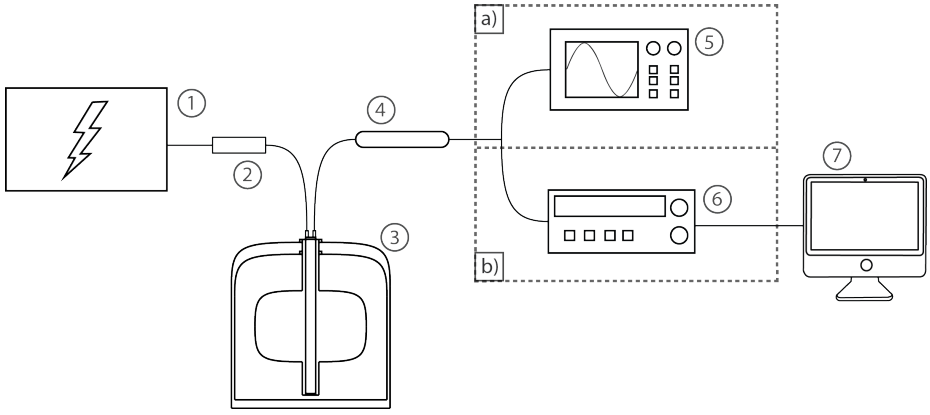

Figure 2.4: Schematic drawing of 1G apparatus. a) Permutation 1: the microwave generator (1) is an SRS Model SG384 gratefully borrowed from Prof. David Hall's Lab; the attenuator stack (2) totals to -29dBm; the sample chamber (3) is the PPMS; the power diode (4) is an HP8472A crystal detector; and the oscilloscope (5) is a Tektronix TDS 1002b. b) Permutation 2: the measurement apparatus here consists of an Agilent 34401A digital multimeter (6) connected to a PC (7) running a LabView data collection routine. (The PC also connects to the PPMS and microwave generator to control the input signal and PPMS magnetic field.)

rapid acquisition time and convenient display makes this use quite natural. The aim in diagnostic viewing is to search out the frequency of a particular resonance, since it is generally unknown within a range of several GHz before testing. The fastest way to do this is to set the RF generator into "sweep mode," which lets it output a series of consecutive frequencies (determined by user) many times per second. The generator then outputs both the main signal and a sawtooth signal at the sweep frequency. The oscilloscope can trigger on the latter signal while measuring the former to display a standing waveform up to several GHz in width, as shown in Fig. 2.5. Such a display lets the user quickly search out interesting response frequencies from the circuit — the most interesting of all being the resonator's resonance peak, which shows up as an exceedingly narrow (MHz order) spike in the window.

Thus the advantage of the 1P apparatus is exactly its speed in observing the circuit's general behavior. The disadvantages are two-fold: one, the oscilloscope is fundamentally imprecise compared to other, slower methods of measurement, and the output signal must be in the high power regime[4] for the oscilloscope to detect it. This latter issue means that resonator displays non-linear behavior, as will be elaborated on below. It suffices to say here that precise measurement in the high power regime do not give us useful information about the resonator.

To get this useful information, we more precisely take data with the 2P apparatus. Since the multimeter is a much more sensitive piece of equipment than the oscilloscope, it can be run in the

[4]This is roughly defined as anything above about -30 dBm at the resonator. The oscilloscope typically needs powers around -10 dBm to be useful.

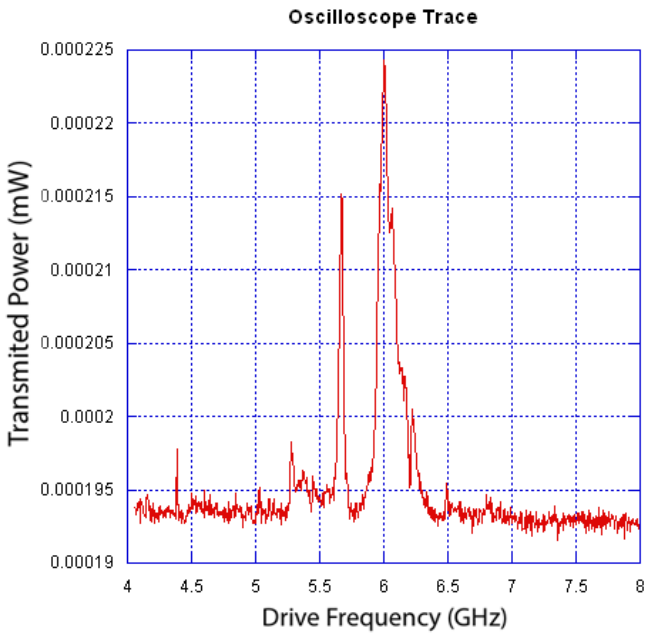

Figure 2.5: Example of oscilloscope background. This is the data visualization we use initially to locate a resonance peak. Note that all of the peaks shown here are likely parasitic resonances, and not due to the resonator, owing to their breadth.

low power regime and avoid the non-linearity problems of the 1P apparatus. The trade-off for this increased precision is a massive increase in the time required to obtain usable data: a single trace of a resonance peak like that in Fig. 2.6 may take between 3 and 10 minutes to complete, depending on the precision level required of the multimeter. Additionally, one must specify a relatively narrow frequency range when running the LabView routine,[5] and so one must have a good idea of the resonance frequency. These issues rule out the 2P apparatus as a diagnostic tool, but it is the only permutation of the 1G apparatus that can collect analyzable data.

To illustrate the non-feasibility of the 1G apparatus for efficiently taking data, we briefly sketch what is necessary to produce the resonance frequency versus magnetic field (FvB) plot, the basic device used to detect sample interaction. An example of this plot is shown in Fig. 2.7, and consists of tracking the resonator's resonance frequency over a series of magnetic fields (produced by the PPMS' solenoid and active in the control zone of the probe cavity). We must first use the 1G1P apparatus to determine the range of frequencies over which to run the LabView routine: we find the resonance frequency at zero-field — this will be the frequency maximum of the FvB plot — and then we find the resonance frequency at the maximum field we are interested in — this will be the

[5]The LabView routine is a nest of loops that can run through iterations in frequency, magnetic field strength, and power. The RF generator cannot be run in swept signal mode with the 1G2P apparatus, and so the program must select each frequency step one by one.

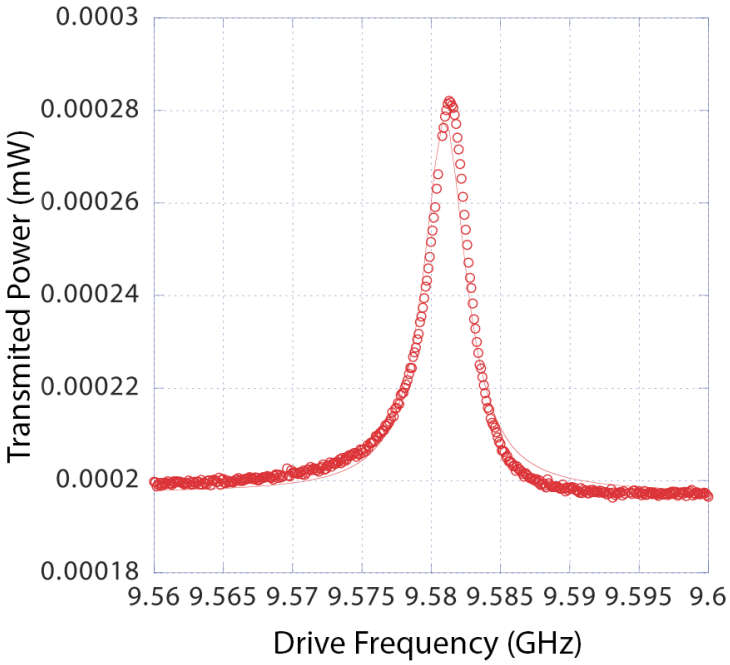

Figure 2.6: A sample resonance peak from the superconducting resonator (no sample mounted). This is considered the raw data of this thesis; i.e. all LabView routines are programmed to produce series of these peaks. This particular curve was taken using the 2G2P apparatus, and so the y-axis is falsely labeled as "power": the raw data is measured in volts, and is then converted to watts using a conversion factor of 400 mW/mV (as provided by the power diode specifications).

frequency minimum. We then switch to the 1G2P apparatus to take the data. After data acquisition, we must fit each trace individually to a Lorentzian curve to extract the interesting parameters of resonance frequency and Q-factor.[6] (If there are parasitic resonances — resonances due to anything other than the resonator — in the vicinity of the resonator's resonance, it may be further required to subtract the background structure from each trace before fitting.) We can finally construct the FvB (or QvB) curve from these parameters. The above process is time consuming and labor intensive, and ultimately hampers the amount of testing that can feasibly be done.

Second Generation (2G)

The solution to most of the problems with the 1G apparatus is simply to automate as many of the tasks as possible, which is the major improvement that the 2G apparatus makes. Each piece of equipment and step of procedure was improved such that measurement became nearly labor free, and the only significant time consideration was that spent averaging data to achieve higher precision.

[6]The Q-factor of a resonance peak is defined as the resonance frequency divided by the peak width at half of its maximum amplitude (FWHM), and measures how damped is an oscillator.

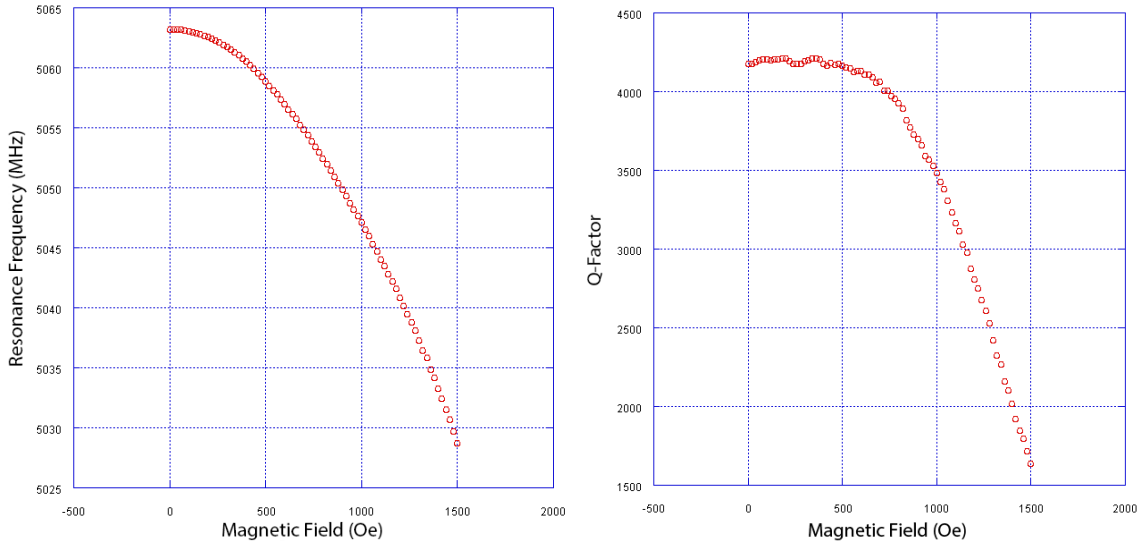

(a) (b)

Figure 2.7: Sample resonance frequency (a) and Q-factor (b) versus magnetic field plots, or FvB and QvB plots. This data was collected with the 2G apparatus at 2.4 K.

The 2G1P apparatus, shown in Fig. 2.8 (a), is nearly identical to the 1G1P apparatus but for the addition of a PC connection to the oscilloscope. By switching the RF generator to a more capable model we are able to dispense with the RF attenuator stack, and we also insert a DC amplifier into the circuit before measurement.[7] The addition of the amplifier does improve the precision of the oscilloscope, but it still must be relegated to a diagnostic role. This capacity has expanded, though, from the 1G1P apparatus because of the addition of the PC running a LabView routine. No longer do the diagnostics need to be manual, and we can gather reams of data quite quickly to get a sense of the resonator's behavior over a range of conditions; FvB and QvB plots can be constructed from the oscilloscope data if we fit it, to give us a preview of what the more precise data might look like.

The 2G2P apparatus, shown in Fig. 2.8 (b), is used for precise data acquisition after the rough peak behavior has been sketched out using the 2G1P apparatus. The principal improvement over the 1G2P apparatus here is the use of a lock-in amplifier in place of the multimeter, which yields a superior signal-to-noise ratio and results in more precise estimates of the resonator's Q-factor and resonance frequency after we fit the data. The lock-in amplifier is no more difficult to use than the multimeter: the RF generator must output an AM signal for the lock-in's reference, which is straightforward, and some trial and error must be done with the lock-in settings. The acquisition time for a series of data such as in Fig. 2.6 depends on the desired precision and the frequency interval

[7]The amplifier is standard op-amp circuit using a OP270 configured with a gain of 10^4.

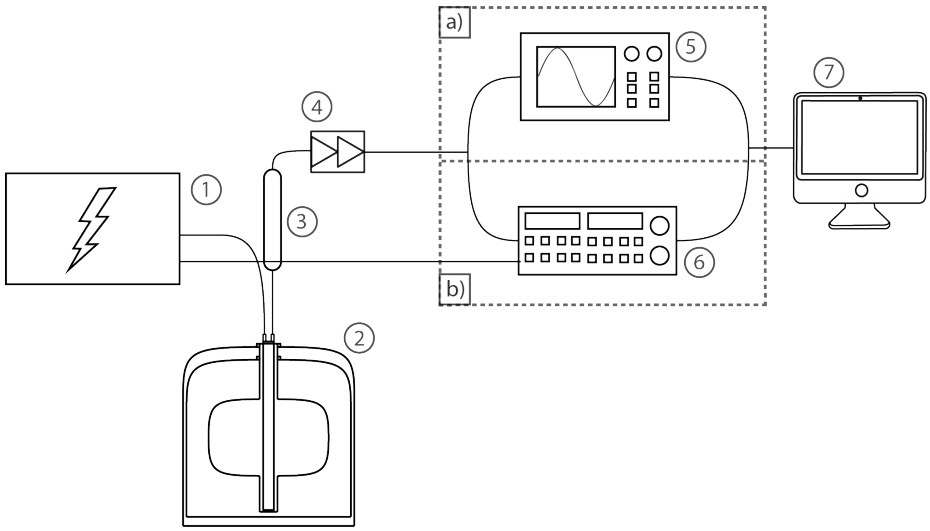

Figure 2.8: Schematic drawing of 2G apparatus. a) Permutation 1: The RF generator (1) outputs directly into the PPMS (2) where the signal passes through the resonator. The signal then is transformed into a DC signal by the power diode (3), is amplified (4), and is fed into the oscilloscope (5), which may or may not be connected to the PC (7). b) Permutation 2: the difference of the 2P apparatus is that measurement is done by a lock-in amplifier (6), not an oscilloscope.

between each data point: the lock-in parameters and LabView settings would be set accordingly.[8] Low precision measurements might take around 2 minutes, while a high precision measurement might take 10 minutes. Note that this is not a dramatic improvement over the time performance of the 1G2P apparatus, although we do have a higher SNR.

What time was not saved with the data acquisition, though, was saved with the LabView routines and data processing procedure. The LabView program is functionally similar to the previous iteration, but includes a peak-tracking feature such that the frequency range for each trace may remain minimal; the LabView program sets the frequency window according to its prediction of where the peak will be located for the relevant conditions. This is not difficult: the peak behavior (previously sketched out with the 2G1P apparatus) is fit to a polynomial function, and LabView centers its window (with a predefined range) on that function.[9] Since a smaller frequency range means less data need be taken, this feature can save much time.

We save even more time by automating the Lorenztian curve fitting process via a Mathematica script. The LabView program for the 2G2P apparatus is set to output its data as a batch of traces

[8]For low precision measurements (typically used for powers between -35 and -30 dBm) we would set the lock-in to have a time constant of 10 ms, and we would pause the RF generator for 30 ms at each frequency; for higher precision measurements (typically used for powers around -40 dBm) we would set the time constant to 300 ms, and we would pause the generator for 700 ms at each frequency. A modulation frequency of 1 kHz was used for nearly all of our experiments.

[9]This method works out in the majority of cases, as the peak behavior in the low power regime is not radically different from its behavior in the high power regime. There are occasional surprises where the LabView window will "lose" the peak, and then this method is not as time-saving as would be hoped.

like that in Fig. 2.6. These are input en masse to the Mathematica script, which processes each in turn, quickly fitting a Lorentzian to each trace and outputting its parameters. An ancillary benefit to the automation of the fitting is that any errors caused by guessing of regression starting parameters is systemized, since the starting parameters are themselves calculated by an algorithm in the Mathematica script.[10]

Third Generation (3G)

Even with the improvements that the 2G apparatus makes over the 1G apparatus, there is still significant room for improvement, and not only in terms of the speed and precision of acquisition: the 1G and 2G apparatuses rely on the power diode to extract the magnitude of power output from the resonator. This method is sufficient to estimate the Q-factor and resonance frequency of the resonator at some precision, but nevertheless ignores much of information carried in the AC signal that could make the estimates better.

What is this information? Since we are interested in the effect of the resonator on the signal, we examine that more closely. In general, a circuit element will change the phase and magnitude of an incident wave, i.e. it will impart a complex transformation. Figure 2.9 shows that this transformation is frequency dependent for the resonator: below resonance the transmitted signal is not appreciably phase shifted and is significantly attenuated; at resonance the phase is shifted by $\pi/2$ radians but not attenuated; and past resonance the phase is shifted by π radians and again is attenuated. This is the well-known classical behavior of a harmonic oscillator, with the familiar phase and amplitude curves shown in Figs. 2.10a and 2.10b.

In general, all of the components in our apparatus — the cables, the power diode, the SMA connectors, the attenuators, etc. — impose their own complex transformations on the input signal, and so the output signal is a convolution of effects. In the 1G and 2G apparatuses, we measure the amplitude of this output and say it is close enough to the behavior of just the resonator, but this is clearly not the case. The aim of the 3G apparatus is to take our accuracy one step forward by isolating the transformation due to the resonator alone and to extract our parameters from just that data.

At this point we direct the reader to Appendix A for a full discussion of how we extract the resonator's transformation, but it suffices to say here that the 3G apparatus must acquire raw complex data to allow the procedure. That is, the apparatus must compare the output signal to the

[10] See Appendix E for the Mathematica program.

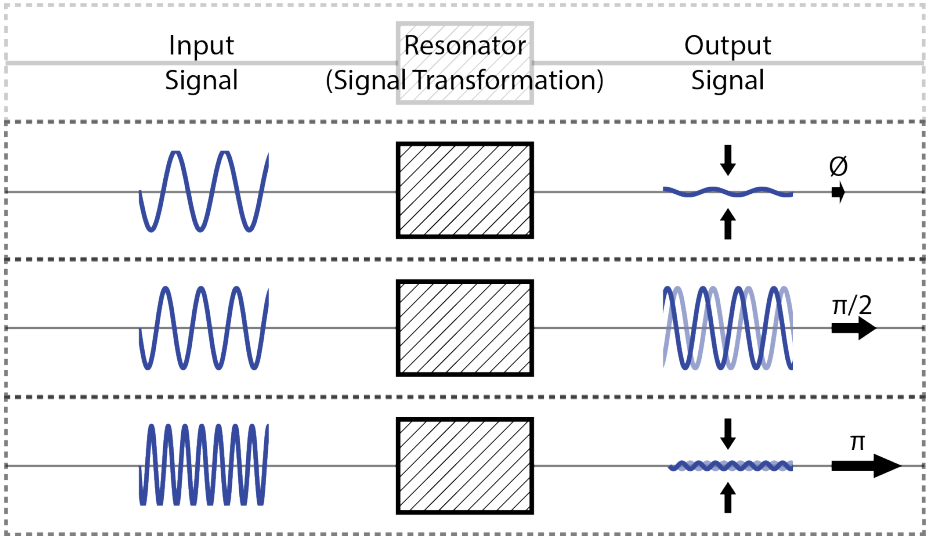

Figure 2.9: Complex signal transformation due to the resonator. The top frame is the below-resonance regime, the middle frame is at resonance, and the bottom frame is the above-resonance regime.

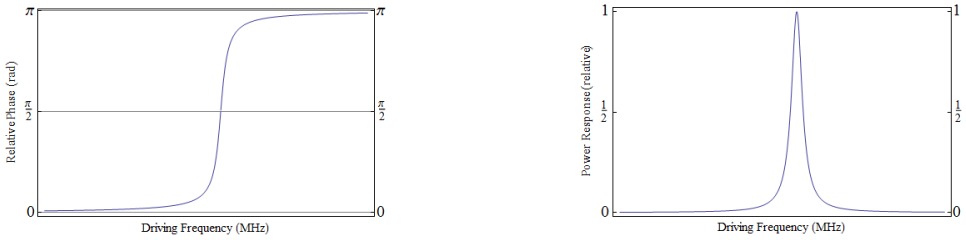

(a) (b)

Figure 2.10: Theoretical phase (a) and amplitude (b) plots for a classical harmonic resonator as a function of driving frequency.

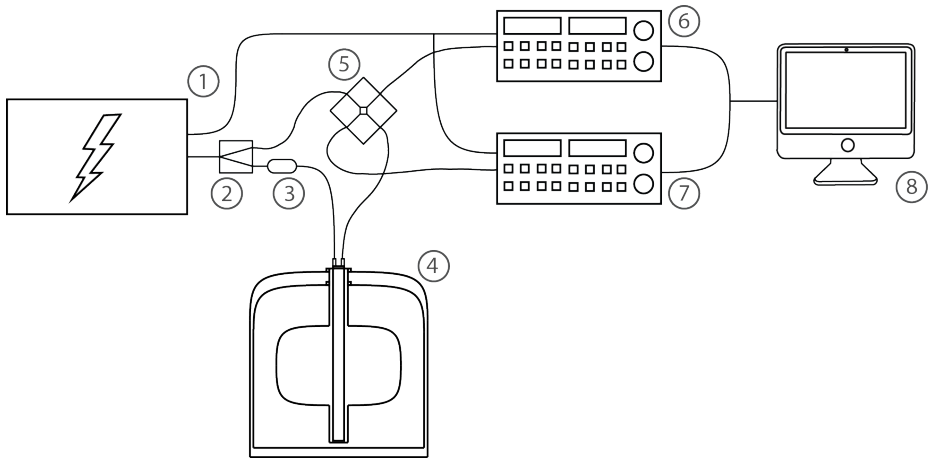

Figure 2.11: Schematic drawing of 3G apparatus. The RF generator (1) outputs the main signal through a splitter (2), with one path leading directly to the IQ mixer (5), and the other first undergoing attenuation (3) and passing through the resonator in the PPMS (4). The IQ mixer outputs to two lock-in amplifiers (6,7) that receive reference signals directly from the RF generator, and they send their data to the PC for processing.

input signal to report both the amplitude transformation and the relative phase transformation.

With this in mind, we take advantage of the IQ mixer to design the 3G apparatus, shown in Fig. 2.11: the output signal from the RF generator is AM modulated and split, with one path leading directly to one input of an IQ mixer, and the other path routing through the resonator before entering the other input of the IQ Mixer. The IQ Mixer outputs an in-phase and an out-of-phase (quadrature) signal, and each is sent to a separate lock-in amplifier.[11] The amplifiers are both locked on to the AM reference signal from the RF generator, and send their output signals to the computer for processing. The entire data collection process, iterating through different magnetic field, power, temperature, etc. settings is automated via LabView routine, as before.

The raw complex data is fit to an ellipse, rotated, and translated into canonical position on the origin to remove the effects of line delay and parasitic resonances, as described in Appendix A. The transformed I and Q data can then be combined into phase and magnitude information and plotted along the lines of Figs. 2.10a and 2.10b. The output from this procedure more or less exactly reproduces the theoretical line shapes, whereas the 1G and 2G apparatuses tended to produce skewed Lorentzian curves due to the convolution of signal transformations.

The relative phase output (Fig. 2.10a) in particular is useful to us, as the resonance frequency is very precisely identified at the inflection point of the arctangent shape. A fitted curve can yield the

[11]The IQ mixer really is the heart of the 3G apparatus. We use it as a homodyne detector to output phase and amplitude information of the signal that passes through the resonator relative to the known output signal from the RF generator. By analyzing its two output signals (I and Q) with the twin lock-in amplifiers, we can reconstruct this information. See Appendix C for a more complete explanation.

resonance frequency with great precision, easily to tens of kilohertz. Instead of fitting the magnitude information as before, then, we modified the Mathematica script for the 3G apparatus to fit lines to the phase information, with the intention of creating hyper-sensitive FvB curves.

Beyond being able to extract more accurate estimates of the resonance parameters, the 3G apparatus achieves an enormous increase in acquisition time at better signal-to-noise ratios compared to the previous generations: in general each data point takes 30 ms to acquire at high precision, whereas the 2G apparatus takes 300-700 ms per datum. Compounding the decrease in acquisition time is an even smaller frequency window for each trace of data: the phase plot has a very narrow resonance feature, and so only a few data points on either side of the feature need to be collected to provide a satisfactory fit.[12]

The better signal-to-noise ratio is guaranteed by a pair of factors: clever use of an attenuator stack, and the use of the IQ Mixer. As to the former, a -20 dBm attenuator stack is in-line with one split of the output signal ((3) in Fig. 2.11), such that one input to the IQ mixer is in the high-power regime while the other input, which passes through the resonator, is in the low-power regime. The combined signals offer the benefits of both: increased signal without the non-linear effects. As to the latter, since the IQ mixer is combining gigahertz range signals, it suppresses noise over a huge bandwidth of lower frequencies.

The 3G apparatus also improves somewhat on the LabView routine, now featuring a real peak-tracking algorithm: the window of each new trace is centered on the resonance frequency of the last trace. Thus, provided that the resonance peak shifts only by a small amount between consecutive traces (such that the new peak location is within the window of the old peak), we obviate the need to perform a diagnostic sweep with the 2G1P apparatus and only need to know the initial location of the resonance peak. All told, the above improvements show that there is no real reason to prefer the 2G over the 3G apparatus.

Procedures

As is detailed in the Introduction and in Appendix B, we expect to observe interaction between the sample spins and the resonator at the magnetic field that satisfies the resonance condition $\omega_{\text{res}}(B) = \omega_{\text{spin}}(B)$, sketched in Fig. 2.12 without coupling, where $\omega_{\text{spin}}(B) = (\text{nonlinear terms}) + (g\mu_0/\hbar)B$ is the sample spins' energy level difference,[13] and $\omega_{\text{res}}(B)$ is the resonator's resonance

[12]The 2G apparatus in general requires a window about 6 MHz wide; the 3G apparatus can operate well with a window as small as 1 MHz.

[13]The nonlinear terms come from anisotropies in the Hamiltonian of the SMM sample; see the Introduction for more information. Note that the linear term predominates at high fields.

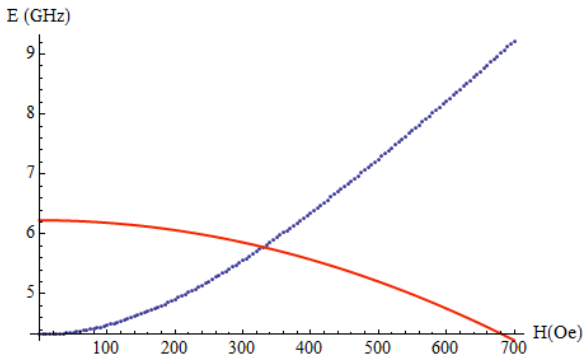

Figure 2.12: Interaction at the intersection of the resonator (red) and sample (blue) resonance conditions. The intersection satisfies $\omega_{\rm res}(B) = \omega_{\rm s}(B)$. Note that this is the same figure shown in Fig. B.2c, except that the resonator deterioration has been amplified by a factor of 500 to provide clarity.

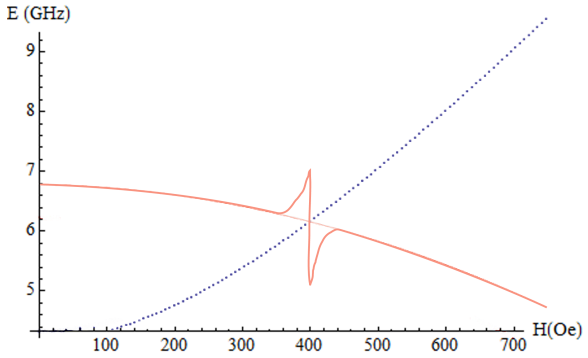

Figure 2.13: Strong coupling between a theoretical SMM sample and resonator: the energy eigenvalues of the strongly coupled system diverge from those of the weakly coupled system shown in Fig. 2.12.

frequency, both functions of magnetic field. Near this point we should see a deviation from the behavior of the uncoupled $\omega_{\rm res}(B)$ due to strong coupling between the SMM sample and the resonator, as shown in Fig. 2.13 [9].[14] Finding an irregularity in the FvB curve of the resonance peak, then, is compelling evidence of sample coupling, especially if it occurs at a predicted magnetic field.[15]

Having described the three apparatuses above, we briefly recapitulate the procedures we use to search for evidence of a mounted sample interacting with the resonator. The 3G apparatus is the preferable apparatus to use for production of an FvB or QvB curve, since it allows more accurate extraction of the resonance parameters than the 2G apparatus, so we will only go over its procedure here; the others are very similar.

With a sample mounted and inside the PPMS, we decide on the range of temperatures, powers,

[14] We also expect a deviation in the behavior of the resonator's Q-factor here, but we focus on the frequency data instead.

[15] See Appendix B for how we may predict the interaction location.

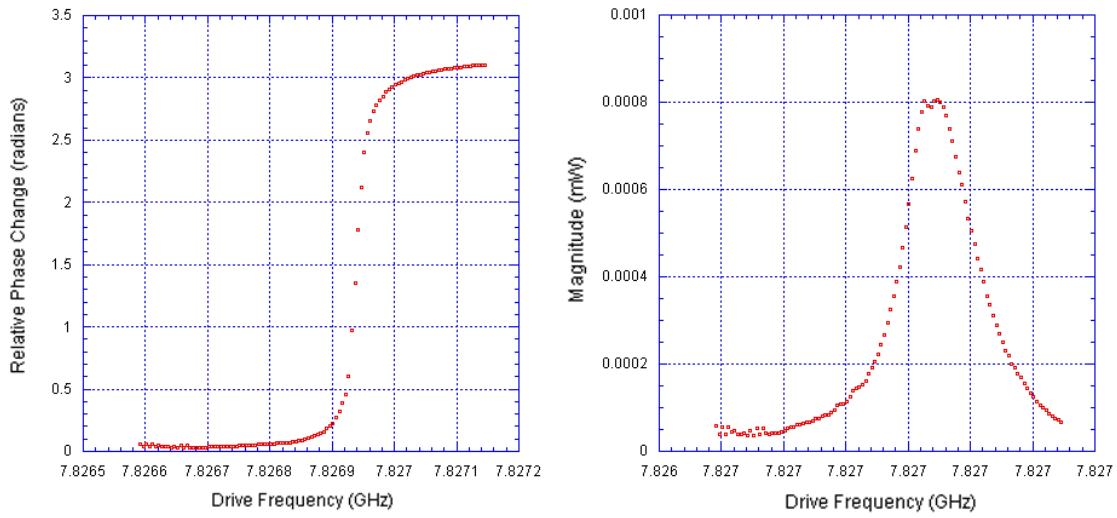

(a) (b)

Figure 2.14: Experimental phase (a) and amplitude (b) plots for one of our resonators (without a sample mounted) versus driving frequency. This data was taken with the 3G apparatus, and is transformed.

and magnetic fields we would like to test over. Because the resonator performance is sensitive to thermal and magnetic conditions, for each combination of temperature and power settings we will need to determine the initial (zero-field) resonance frequency of the resonator using the 2G1P apparatus.[16] A more thorough diagnosis is usually not required since the 3G LabView program is able to track the peak dynamically as it iterates through the prescribed magnetic fields.

The 3G LabView routine outputs complex datasets that can be transformed, as detailed in Appendix A, into the isolated amplitude and phase transformations due to the resonator. An example of this output is shown in Fig. 2.14; it is quite similar to the theoretical curves in Fig. 2.10. The 3G Mathematica script batch-fits the sets of phase information to extract the resonance parameters of interest, and directly outputs both a table of parameters per magnetic field and the FvB and QvB curves.[17]

As noted before, both the Q-factor and resonance frequency are appropriate parameters to track when looking for a sample spin interaction. Anything deviating from the smooth curves like those in Fig. 2.7 warrants careful investigation. Of course, we want to avoid tracking down features that are due to noise or parasitic resonances in the circuit. We can test whether or not a feature is due

[16] Additionally, every time that the resonator is taken out of the PPMS and reinserted later, the peak search must be performed again, even if the thermal and magnetic conditions have not changed. The resonance frequency is sensitive to minute mechanical perturbations of the probe connections, and very sensitive to any shifting of the resonator in its circuit board bed.

[17] See Appendix A for more information on how the fitting is done. See Appendix E for the Mathematica script.

to sample interaction by averaging tests to reduce noise,[18] and/or by resetting the probe to shift parasitic resonances.[19]

The general behavior of the Q-factor and resonance frequency according to the magnetic field remains the same across different temperatures and powers, but the exact slopes and intercepts do vary in predictable ways. These effects are discussed in detail in Chapter 5.

[18] Avoiding false positives is one of the primary motivations for increasing the apparatus' SNR.
[19] See Appendix B for more detail on this prediction.

Chapter 3

Preliminary Results and Superconductivity Theory

So far we have described the significant technology improvements we made over the course of this research, but we have also seen that what separates the 1G and 3G apparatuses from a practical standpoint is only their convenience and accuracy. Although the complex transmission data acquired by the 3G apparatus gives faster and more accurate characterizations, the observation of sample-resonator interaction should be visible using either apparatus. Indeed, Adams reported some success with the 1G apparatus in his thesis [2]. The first period of research, in which we attempted to replicate Adams' research, was marred, though, by unusable data: we were able to successfully characterize resonance peaks (and so able to track their parameters across magnetic fields), but we were not able to sustain these peaks into high magnetic fields. Furthermore, the behavior of the peaks and their parameters were not as predicted as magnetic field increased. Instead of the smooth curves we showed in Chapter 2 Section 2, we obtained the broken curves of Fig. 3.1.

With unexpected and non-reproducible features appearing in our data without a sample mounted to the resonator, our ability to identify a particular feature as being due to a sample spin interaction was dubious. Additionally, without being able to enter into higher field territory because of resonance peak degradation, certain samples were effectively off-limits to our exploration.[1] Our primary research of characterizing sample interactions thus had to pause as we searched for ways to modify the apparatus and procedure so as to recreate the FvB and QvB plots expected by the literature and by Adams' experience.

[1] See the Introduction for a small discussion on how resonators are chosen for a particular sample.

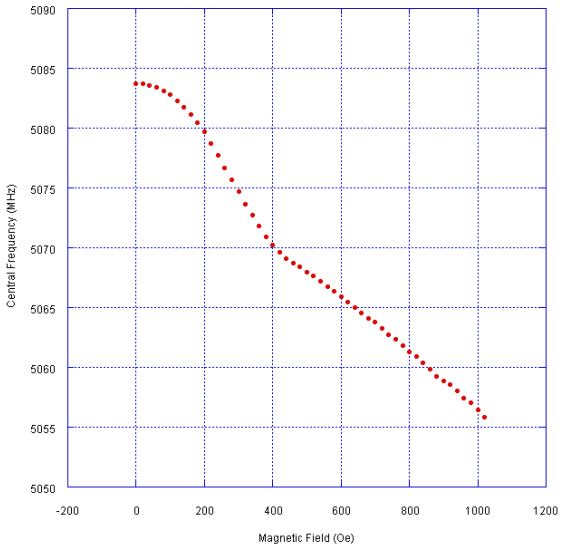

Figure 3.1: Example of an FvB curve affected by flux trapping. Such a curve is characterized by the low-field curvature pattern negative-positive-negative. This should be compared to the ideal behavior in Fig. 2.7, where curvature is uniformly negative.

Initial brainstorming to locate the issues causing poor performance centered both on imperfections in the construction of the apparatus — for example, faulty SMA connectors, improper impedance matching, defective wire bonds connecting the resonator to the circuit board — and on imperfections in the PPMS environment — for example, ice in the sample chamber, stray or misaligned magnetic fields in the control zone, degradation of the niobium surface of the resonator, or excessive magnetic flux trapping in the resonator. Through diagnostic testing and analysis of the results,[2] we were able to pinpoint the problem to be excessive flux trapping due to the imperfect alignment of the resonator relative to the magnetic field in the PPMS: for minimal flux trapping the resonator should be parallel to the magnetic field, but the probe then being used had the capacity neither to modify nor to measure the angle of the resonator inside the PPMS.

Before we discuss the solution to this problem, i.e. the redesign of the probe to combat flux trapping, we will discuss in the following section what exactly is flux trapping and why it produces unfavorable results such as those in Fig. 3.1.

[2]See Chapter 4 Section 4 for an overview of these testing techniques.

Superconductivity Theory[3]

After nearly a century of research and consistent innovation through the development of the London equations, BCS theory, Ginzburg-Landau theory, etc., superconductors have become well-described physical systems. Their properties of perfect conductivity (no resistance to current flow) and perfect diamagnetism (the Meissner effect — no bulk penetration of external magnetic fields) are known even outside of the sciences.

The obvious reason for our choice of niobium as the resonator material are its superconducting properties: niobium has the highest critical temperature of any of the pure metals ($T_c = 9.26$ K), and so it can be counted on to maintain a superconducting current through the temperatures we use (between 1.8 K and 4 K). The implication for the experiment of having a resistance-free current in the resonator is mainly that the Q-factor of the resonator can be much higher, and this is crucial as we are trying to detect small shifting of the resonance frequency.

Thus the niobium superconducting resonator seems very convenient to use, but we also recall its limitations: superconductors are characterized by both a critical field, H_c, and a critical current, I_c; if the field or current exceeds these limits, superconductivity is broken, and the desirable effect of perfect conductivity is lost (there exists also, of course, the critical temperature, T_c)[4]. Keeping in mind that the motivation of this section is to understand magnetic flux trapping, we explore why the phase of the superconductor changes from superconducting to normal (i.e. non-superconducting) at these limits.

We first consider an argument in terms of energetics. The formation of Cooper pairs permits the charge-carrying electrons to collapse into a single low energy state, which is normally prohibited by the Pauli exclusion principle. (This is because Cooper pairs behave as bosons instead of fermions, and so obey Bose-Einstein statistics.) There is thus an energy savings from entering the superconducting phase. There is a competing energy cost, however, when the superconductor is exposed to external magnetic fields. To preserve perfect diamagnetism inside the bulk of the superconducting material, surface currents[5] must be formed to "screen" the rest of the material: since the surface

[3]Much of this section is due to Kresin and Wolf's *Fundamentals of Superconductivity* [15] and to Tinkham's *Introduction to Superconductivity* [26].

[4]T_c is the temperature below which the thermal noise in a material becomes low enough to allow electrons to form Cooper pairs.

[5]This is the Meissner effect, the expulsion of magnetic fields from the interior of a superconductor's bulk at low fields, currents, and temperatures (such that each is below its critical value), which is effected by responsive currents residing on the surface of the superconductor. These currents create magnetic fields in exactly the configuration required to "cancel" the external magnetic fields that would penetrate the superconductor's bulk. We note that the expulsion of magnetic fields is not perfect; there is a penetration depth, δ_λ, (the subscript λ is a reference to the London equations) through which the external magnetic field decays; the decay of the field within the superconductor can usually be described exponentially, and δ_λ in that case is said to be the distance over which H reduces by e. For intuition's sake, δ_λ is usually a few hundred Angstroms.

of a superconductor is in a normal phase, maintenance of these currents imposes an energy cost. Beneath T_c, then, superconductivity is maintained until the external field becomes so strong as to render the energy costs of maintaining diamagnetism greater than the energy savings of maintaining Cooper pairs: the material switches to the normal phase and the magnetic field penetrates the bulk.

We consider further that there might be an intermediate energy "mixed state" wherein the external magnetic field is only *partially* penetrating the superconducting material. In fact, the description of the mixed state is one of the major triumphs of the Ginzburg-Landau theory, which is able to describe the Cooper pair density $n_s = |\psi|^2$ close to the surface, and so determine the intermingling of superconducting and normal states. The results of the theory are the differential equation for the "pseudo-wavefunction" of Cooper pairs, ψ,

$$\frac{1}{2m}(-i\hbar\nabla - e\mathbf{A})^2\psi + \beta|\psi|^2\psi = -\alpha(T)\psi \tag{3.1}$$

and the equation of the "supercurrent,"

$$\mathbf{J}_s = \frac{e\hbar}{2im}\left(\psi * \nabla\psi - \psi\nabla\psi*\right) - \frac{e^2}{m}|\psi|^2\mathbf{A}, \tag{3.2}$$

where $\mathbf{A}$ is the magnetic vector potential, e is the electron charge, m is an effective mass, and α and β are experimental parameters [15].

Abrikosov was the first to notice that there would be a fundamental change in behavior of superconducting materials according to these equations dependent upon the ratio $\frac{\delta_\lambda}{\xi}$, where δ_λ is the penetration depth of the external magnetic field, and ξ is the correlation length of the Cooper pairs.[6] On the basis of these two parameters, we divide superconductors into two types: Type I and Type II, defined respectively as having $\kappa = \frac{\delta_\lambda}{\xi} < \frac{1}{\sqrt{2}}$ and $\kappa > \frac{1}{\sqrt{2}}$. (Note that niobium, the material of our resonators, is a Type II superconductor.)[7] The difference in behavior can be qualitatively understood from the diagram in Fig. 3.2, which is derived from the Ginzburg-Landau equations above.

The figure shows a superconducting domain diagram, where the two domains are sketched with respect to x, the distance from the superconductor's surface. The bulk of the superconductor is in the superconducting phase, where there is a high density of Cooper pairs. As we approach the surface this density decreases with the characteristic length ξ, and at the same time the magnetic field begins to increase with the characteristic length δ_λ. As the diagram shows, these regions may intersect to

[6] Intuitively, this is related to the spatial separation between electrons in the Cooper pair.

[7] The relation for κ may differ by a constant from what is presented, with a corresponding change in the cutoff point between Type I and Type II superconductors.

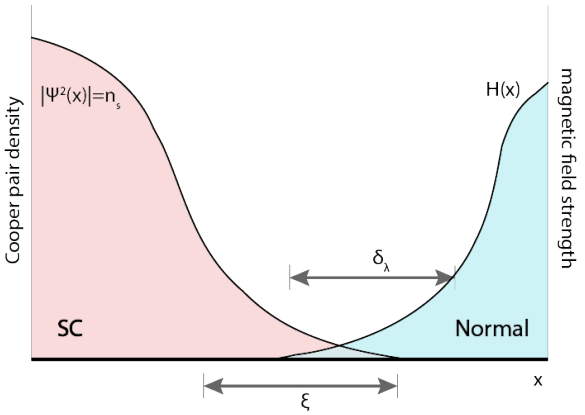

Figure 3.2: Superconducting domain diagram. This diagram represents the near-surface area of a bulk superconductor, with position represented on the horizontal axis. The surface exists in the normal phase, and the interior exists in the superconducting phase. These phases can coexist in a "mixed state" where they overlap. The left-hand curve represents the diminishing Cooper pair density as the surface is approached, and the right-hand curve represents the decaying external magnetic field as the surface is departed from.

form the mixed state, the state in which both phases may coexist. For Type I superconductors with $\delta_\lambda < \xi$, the magnetic field does not penetrate very far into the superconductor, and so there is no overlapping of superconducting and normal regions: no mixed state is formed. For Type II superconductors with $\delta_\lambda > \xi$, the superconducting and normal regions do overlap because of the further penetration depth of the magnetic field.

To extend this argument as it relates to H_c, a Type I superconductor will have an abrupt phase change between the superconducting and normal domains, and that occurs at H_c. A Type II superconductor has two phase changes, represented by H_{cl} and H_{cu}: respectively the "lower critical field," which separates the superconducting domain from the mixed state, and the "upper critical field," which separates the mixed state from the normal domain. Between H_{cl} and H_{cu} the magnetic properties of the superconductor transition smoothly between those of the pure superconducting domain and those of the pure normal domain, although the bulk superconductor maintains zero resistance to electric current throughout. This behavior is captured in Fig. 3.3. It is this domain mixing between H_{cl} and H_{cu} for Type II superconductors that we want to investigate.

We take as our starting point a Type II superconductor below T_c at low field; it is firmly within the superconducting domain. As we raise the external magnetic field to just above H_{cl}, some magnetic field penetrates the superconductor to form a mixed state. Peculiarly, the penetration is not laminar, but tubular: a flux line will go straight through the bulk of the superconductor. There is a Lorentz interaction between the electrons of the bulk material and the penetrating magnetic field: those electrons with velocities normal to the penetration will circulate around the field lines,

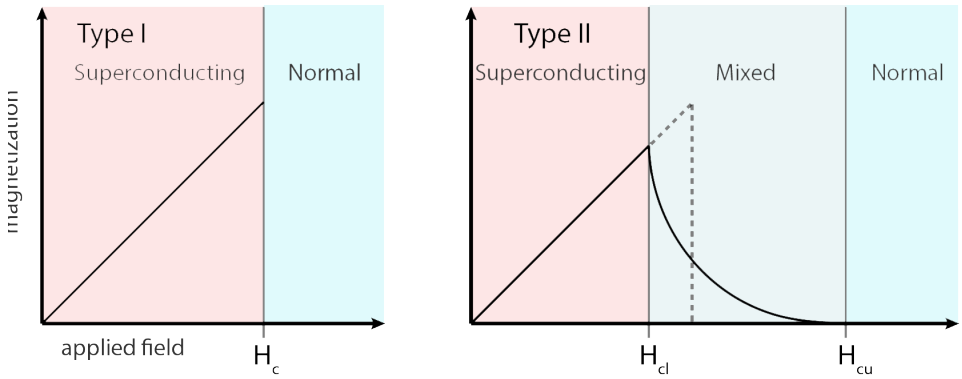

Figure 3.3: Critical field differences between Type I and Type II superconductors.

forming "vortices". In the core of a vortex the electrons whirl around so quickly as to destroy the superconductivity conditions, and so the vortex lines exist as islands of normal phase matter in the bulk of the superconductor.[8] As we continue to increase the external magnetic field, more and more vortex lines of "trapped magnetic flux" form, eventually creating a triangular lattice of phase-normal perforations through the superconductor. As the external field reaches H_{cu}, the vortex lattice becomes so dense as to collapse the entire bulk into the normal domain, and superconductivity ceases.[9]

For practical uses of a Type II superconductor, such as our niobium resonator, these vortex lines are of great significance because of the dissipative effects associated with them. In our experiments we couple a current through the resonator and rely on the superconducting properties of niobium to generate a resonance peak with a very high Q-factor. Ideally, the flow of current would be resistance-free, but this perfect superconductivity only occurs at the low field, zero frequency limit: some resistance to flow inevitably develops at non-zero frequency, and as soon as we surpass H_{cl} penetrating magnetic flux lines will develop in our resonator.

Given a uniform bulk superconductor, these flux lines will develop Abrikosov vortex currents around them. If we then apply a bias current across the superconductor perpendicular to the magnetic flux lines — as we do with our resonator in the experiment — a Lorentz force acts between the bias current and magnetic flux lines. The vortices must then begin to move through the superconductor, perpendicularly to the bias current, and they will oscillate if the bias current is oscillatory — again, as it is during our experiment. The movement of Abrikosov vortices leads to energy losses through at least two mechanisms. The first: as a vortex moves through the superconductor lattice, its

[8] It is interesting, though not quite relevant to the discussion, to note that the magnetic flux lines are quantized; each vortex only supports $\frac{hc}{q_e}$ units of flux [8].

[9] In the domain between H_{cl} and H_{cu} the bulk of matter is still considered superconducting despite the presence of normal-mode vortex lines. The spaces between vortices still are diamagnetic and perfectly conducting.

normal-phase electrons interact with the thermal vibrations of the lattice, and there is an associated Joule heating; and the second: the vortex of normal-phase electrons must move through the bulk of superconducting-phase electrons, and there will inevitably be an interaction, the "normalization" of electrons at the leading edge of the moving vortex [15].

The above dissipative mechanisms depress the Q-factor and resonance frequency of our resonator, and so makes our characterization of the resonance peak more difficult. It is thus in our interest to minimize these effects. One interesting way to do this is to introduce impurities into the superconductor bulk. When vortices form due to a partially penetrating magnetic field, they will tend to form on these impurities, which are locked to the crystal lattice of the superconductor. A small applied current, then, will be unable to move the vortex since it is "pinned" to the crystal lattice, and therefore dissipative effects are mitigated. This trick only works up to some critical current, where the Lorentz interaction between the current and trapped flux becomes large enough to depin the vortex. Such impurities in the context of superconducting film resonators (like the CPWG resonators we use) are usually small holes punched through the superconducting film in strategic locations, and are called "antidots". Bothner et al. have had considerable success in implementing antidots on their superconducting CPWG resonators [5].

Another possibility of minimizing the dissipative effects of the Abrikosov vortices is the use of thin-film superconducting resonators. We take into consideration two factors: one, that Abrikosov vortices form due to partial magnetic field penetration being energetically favorable to fully-screening surface currents, and two, that an Abrikosov vortex has a defined dimensionality due to the magnetic flux quantization condition, i.e. it has a minimum size. We thus make two arguments for the thin-film resonator:[10] the first, that for a thin-enough film the London penetration depth δ_λ is longer than the resonator is wide, and so non-tunneling flux will penetrate the entire thin-film, obviating the energy advantages of a vortex; and the second, that for a thin enough film there will be insufficient space for a vortex to form. There is the obvious disadvantage to this approach that there will be no superconducting regions in the thin-film if the entire body is penetrated by magnetic flux.

A third solution, which we chose to pursue and which we discuss in the following chapter, is to limit exposure to the magnetic field by turning the plane of the resonator parallel to the incident magnetic field. This orientation minimizes the projection of the resonator's surface normal to the magnetic field lines, and so minimizes magnetic flux. With a minimum of magnetic flux, it follows that trapped magnetic flux, and the resultant vortices, will be minimized as well.

[10] We are here assuming that the external magnetic field is applied parallel to the plane of the thin-film.

Chapter 4

Probe Design

Having established the problem with the probe inherited from Adams — the resonator was trapping too much magnetic flux — a few ideas were floated to counter it. The three most practicable solutions were: one, the refabrication of the resonators with microdots lining the waveguide; two, refabrication of the resonators with a thinner substrate of niobium; and three, manipulating the angle of the resonator inside the PPMS sample space to align it as parallel as possible to the magnetic field.[1] Because it did not require undertaking the lengthy process of making new resonators, and because it would likely need to be done anyway to maximize the benefits from the first and second proposals, the third proposal was chosen as the first course of action: the probe had to be redesigned.

In presenting our probe design, we will pass over the many iterations that we implemented throughout the research and present only the final design. We first overview the constraints of the problem.

Constraints

The Physical Property Measurement System (PPMS) that we use for this research, although it offers us very convenient control over the temperature and magnetic field in its control region (the region of calibrated and homogeneous fields and temperature), nevertheless imposes substantial spatial constraints on the design of the probe. Referring to the PPMS diagram in Fig. 2.2, we see that the probe cavity is a long cylindrical hollow that plunges from the top of the PPMS through to the control region. The control region is about 2.5 cm in diameter and 5.5 cm in height, and it is centered about 5.1 cm from the base of the probe cavity and 100 cm from the top of the

[1] Refer to Chapter 3 Section 3 for the motivation behind these proposals.

cavity. Any practical probe design, then, must form a hermetic seal at the top of the cavity[2] and run cabling down to the resonator, which must be supported within the control zone. Because the PPMS produces a magnetic field parallel to the long axis of the probe cavity, the resonator should be held such that its plane is also parallel to the long axis of the control zone. We additionally note here that because we run transmission ESR, cabling will necessarily need to form a loop after it passes through the resonator such that the signal may travel back up and through the probe's top plate.

In addition to these geometric constraints, the ambient conditions inside the probe cavity place further restrictions on the probe design, mostly in the consideration of materials allowed in construction. The temperature in the control zone may range from 1.8 K to 315 K, over the span of which most materials naturally expand or contract substantially; to allow the PPMS temperature to function properly it is also desirable to thermally insulate the control region from the rest of the probe cavity, and above all not to allow easy conduction channels from the control zone to the laboratory space by means of the probe. Because the experiment is very sensitive to magnetic fields around the resonator, non-magnetic materials must be used in its vicinity, which further constraints us. Additionally, the high frequency AC signals we use during the experiment — typically between 4 and 8 GHz — necessitate selection of cabling that will not be too lossy over this band.

These are only the constraints that the PPMS and our particular experiment imply. We furthermore must design our probe to solve the flux trapping problem: we need to be able to manipulate the angle of the resonator, ideally *in situ*. We prefer *in situ* for two reasons: one, that we cannot be sure that the magnetic fields inside the PPMS are properly calibrated, and so aligning the resonator with the probe axis may prove insufficient; and two, a resonator orientation aligned outside the PPMS may not remain the same once inside the PPMS, presumably due to differential thermal contractions. So, we have to design a mechanism that swings the resonator through several degrees of rotation, that fits within the limited cavity space, and that also is manipulable from outside the PPMS.[3]

We impose one additional constraint, or at least a strong consideration, to the design: the niobium resonators we use are specifically designed to be mounted via wire bonds to a complementary circuit board (Fig. 4.1), and so it makes utmost sense to respect this aspect of the design, i.e. to maintain the resonator on its current circuit board.[4] Since the resonator lies flat within the bed of the circuit

[2]The cavity is filled with helium during operation.

[3]If the reader is curious at this point how we might discern the angle of the resonator once it is inside the PPMS, we point to Section 4.

[4]See Appendix D for descriptions of the resonator and circuit board.

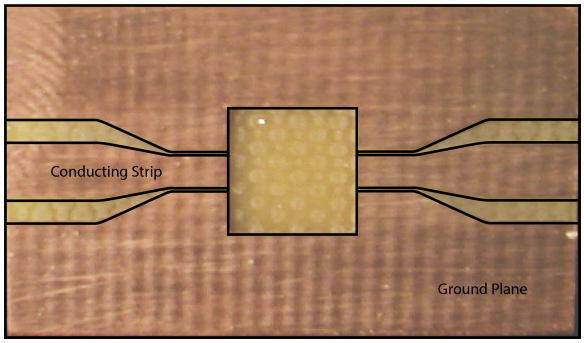

Figure 4.1: The circuit board designed by Adams to hold the niobium resonators. The resonator sits on a thin layer of vacuum grease in the central dugout and is electrically connected to the ground plane and conducting strips via aluminum wire bonds. The geometry of the CB is made to impedance match the resonators we use. For more information, see Appendix D.

board,[5] it will suffice to design a probe that allows the alignment of the circuit board, henceforth referred to as the CB.

We recapitulate the design constraints: the entire probe must fit into the cylinder of the probe cavity, and it must suspend the CB inside the control space; the probe must not excessively conduct heat along its length, and it must be manufactured from non-magnetic materials in the vicinity of the resonator; also the probe must incorporate a mechanism, controllable from outside the PPMS, to adjust the angle of the CB.

Design

Again, we will only present the final design iteration below.[6] The portion of the probe that is suspended into the control zone is pictured in Fig. 4.2 in both assembled and exploded forms. The rest of the probe consists of the pictured two co-axial cables and the green control rod as they stretch to reach and penetrate the top of the probe cavity,[7] as well as three circular baffles that slip around the cables and rod and provide structural rigidity along the length of the probe. The figure shows the major constituents of the assembly: the CB carriage, the CB holder, the co-axial cables, and the gear mechanism, including the control rod. We will examine each of these elements in turn to show how they satisfy the design constraints.

The CB carriage, pictured in detail in Fig. 4.3, is meant to maintain good electrical and mechan-

[5] In fact, the resonator can be made to lie at a slight angle within the CB dugout by mounding the vacuum grease underneath it. This can be quite useful if we find that the probe rotation mechanism is not quite reaching the desired (parallel) angle; in that case we may purposefully bias the resonator's angle on the CB to ensure proper alignment.

[6] Many grateful thanks are given to Jim Kubasek for his collaboration in designing the final probe, for his work in machining the parts, and for his generosity in putting together the drawings.

[7] Each of these, the two cables and the control rod, pass through hermetic bulkhead connectors at the probe cap.

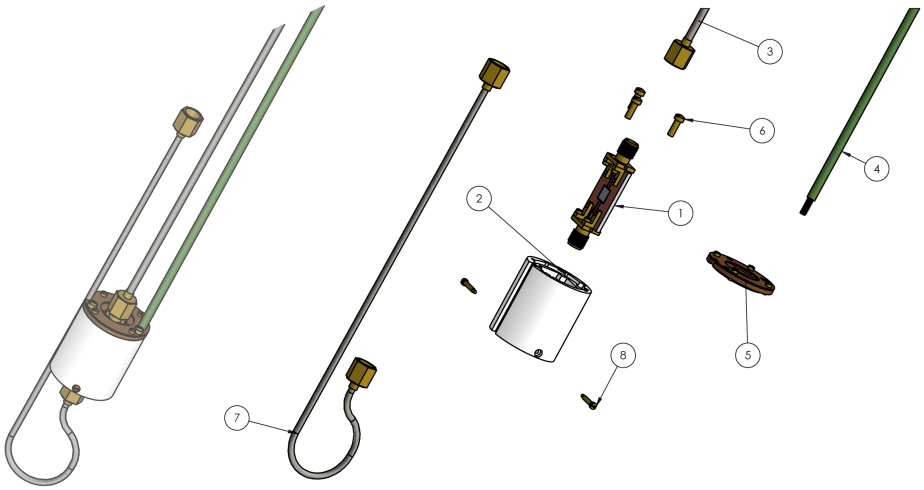

Figure 4.2: Drawing of the probe assembly. (1) is the CB carriage; (2) is the CB holder; (3) & (7) are non-magnetic, semi-rigid copper coaxial cable (Tek-Stock, UT-085C-LL); (4) is threaded G10 control rod (.125" diameter, 2-56 thread on last .25"); (5) is the gear mechanism; (6) is a 2-56 x .25" brass screw to affix the gear mechanism to the CB holder; and (8) is a pivot screw to restrain the CB carriage within the CB holder.

ical contact between the transmission lines and the CB. This role is complicated, as we will soon describe, by the significant torque applied by the transmission lines to the CB. The basic structure of the carriage is of two brass SMA jacks attached via brass brackets by brass through-screws to the CB ground plane. To be certain of good electrical contact between the center pins of the SMA jacks and the center strip line of the CB, we sandwich a sliver of soft indium metal in-between the pin and the CB.[8] This connection method deviates from the standard practice of mechanically clamping the SMA jacks to the CB surface with fingers extending from the back of the jack, a technique which failed to adequately secure the connectors during CB rotation, and it also proved superior to attempts at cementing the jacks to the CB surface with silver epoxy. Note that the choice of brass for the jacks, brackets, and screws is non-magnetic, and so the components should not interfere with measurements during operation.

The CB carriage sits inside the CB holder, pictured in Fig. 4.4, the purpose of which is two-fold: to serve as an anchor for the rest of the probe components, and to constrain the CB carriage to only one axis of rotation. We ensure this second point by designing the holder as a solid cylindrical slug with a wedge shaped cavity to accept the carriage. (Holes are located at the top and bottom of the holder for the transmission lines to pass through.) The wedge is precisely dimensioned such that there is no room for translation of the carriage within, and its rotation is constrained to the axis

[8]This technique may result in some impedance mismatching, and thus may cause some of the resonance peak distortion we see during the experiment.

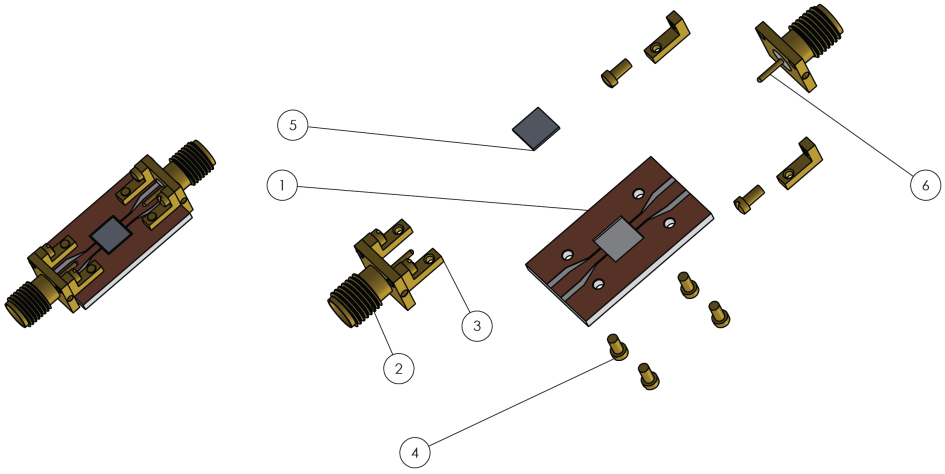

Figure 4.3: Drawing of the CB carriage. (1) is the circuit board, drilled to accept the bracket connectors (copper clad ceramic, Rogers Corp., R04350B); (2) is the modified brass SMA connector; (3) is the brass bracket used to affix the SMA connector to the CB;(4) is the brass screw used to connect the circuit board to the bracket; (5) is the superconducting niobium CPWG resonator; (6) is the central conducting pin of the SMA connector, which rests on top of the CB's central conducting strip.

parallel to the sharp of the wedge. (This is illustrated in Fig. 4.5.) The outer diameter of the slug is designed to fit snugly in the probe cavity at room temperature, although it contracts slightly as the temperature reaches 1.8 K. The snug fit is necessary since the manipulating mechanism applies force between the carriage and the holder: the holder must remain motionless (or nearly so) so that we can be certain that the carriage and not the holder is sweeping out a rotation. The CB holder has a set of screw holes near its base that lines up with a set of screw holes in the lower SMA jack of the carriage: when connected with a set of brass screws, a robust rotational axis is formed. (Again, see Fig. 4.5.) Additionally, a channel is cut along the outside length of one side of the holder so that the transmission line can pass by; cutouts to house the gear mechanism are also present on the upper side of the holder.

The transmission lines are divided into four lengths: two straight sections extend from the probe cap to about 10 cm above the CB holder, and the other two sections, one straight and one hooked as shown in Fig. 4.2 link the upper lines to the CB carriage. Because of the high frequency AC signals we use, the transmission lines were chosen to be semi-rigid coaxial cables notable for their low loss. The upper two cables, constrained to be poor thermal conductors, are stainless steel, and the lower two cables, which must be non-magnetic, are made from copper. The connections between the two sets of cables are made from pairs of non-magnetic brass SMA connectors. Finally, the hook of the lower SMA cable is over-sprung, i.e. it is bent such that when connected to the carriage, the

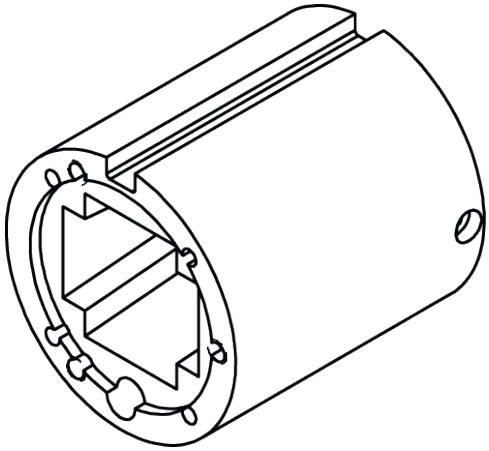

Figure 4.4: Drawing of the CB holder. The holder is a 3D printed solid, designed in AutoCAD.

CB is torqued against the wall of the wedge closest to the transmission line channel. In this way the transmission lines themselves provide a restoring torque for the carriage that opposes the active torque applied by the gear mechanism. This means that the control mechanism need only be able to apply force in one direction in order to rotate the CB in two directions (a reduction of applied force will result in opposite rotation).

The gear cartridge, shown in Fig. 4.6, is what manipulates the angle of the CB carriage. Since the carriage is biased towards the cable channel, the control mechanism practically only needs to pull the carriage away from the wedge face close to that channel. And because the holder is kept stationary by its full diameter pressing against the probe cavity walls, it suffices to move the upper SMA jack of the carriage relative to the holder. Thus we plant the cartridge on top of the holder and pass the upper jack through the central hole of the gears. This hole is an off-center cutout from the central ring gear: when the ring gear rotates, so too does the hole, and the hole is positioned and sized such that its movement forces the captive SMA jack to also move. Since the jack is confined to one degree of rotation, it only moves in the desired directions despite the circular motion of the gear's hole. The drive gear ((5) in Fig. 4.6), also residing in the gear cartridge, translates rotations of the control rod into rotations of the ring gear with a ratio of 1:4. The control rod extends from the drive gear through a hermetic bulkhead connector in the probe cap and terminates in a knob for easy manipulation by the experimenter.[9] The material of the cartridge and its screws is entirely bronze, so as not to interact magnetically with the experiment, and the control rod is G10 plastic, which is

[9]The center of the drive gear is threaded, as is the end of the drive shaft, such that the experimenter can simply screw the drive shaft into the gear. Once enough threads are engaged between gear and shaft, friction forces additional drive shaft rotation to translate into drive gear rotation instead of continued threading. To allow both CW and CCW rotation of the drive gear without unthreading the drive shaft, vacuum grease is applied to the threads: at low temperatures the grease vitrifies, essentially acting as a glue between shaft and gear.

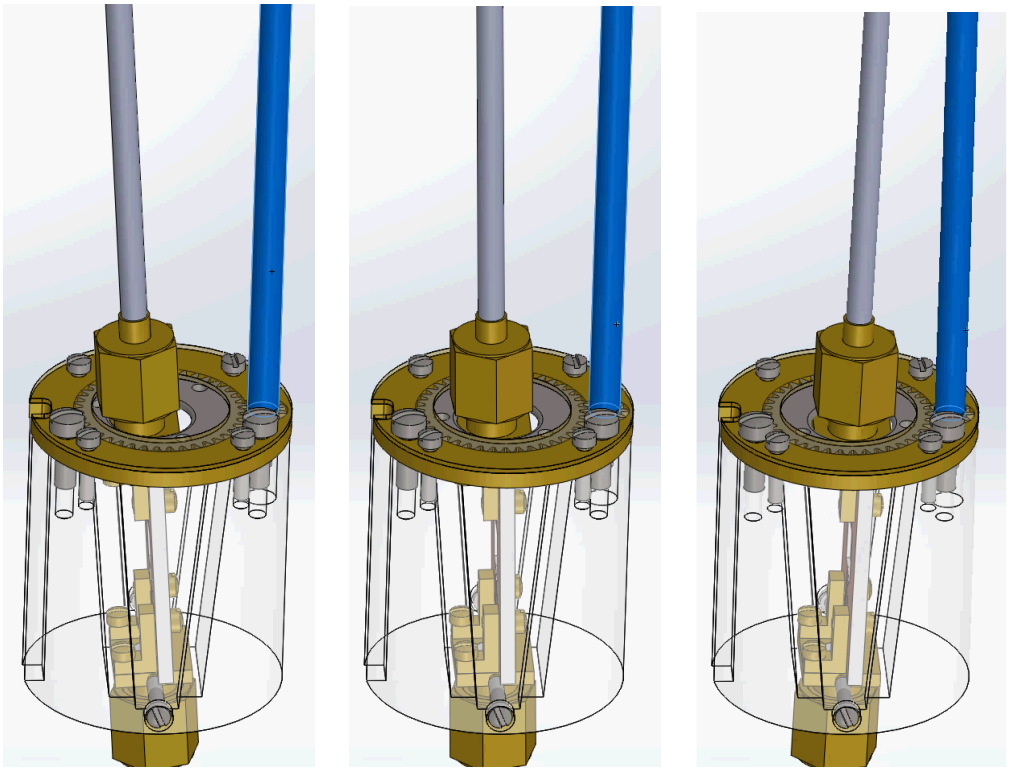

(a) (b) (c)

Figure 4.5: Rotation of the carriage within the holder. Twisting the control rod (blue) clockwise will rotate the carriage through frames (a), (b), and (c), then back through (b) and (a) to complete a full rotation of the ring gear.

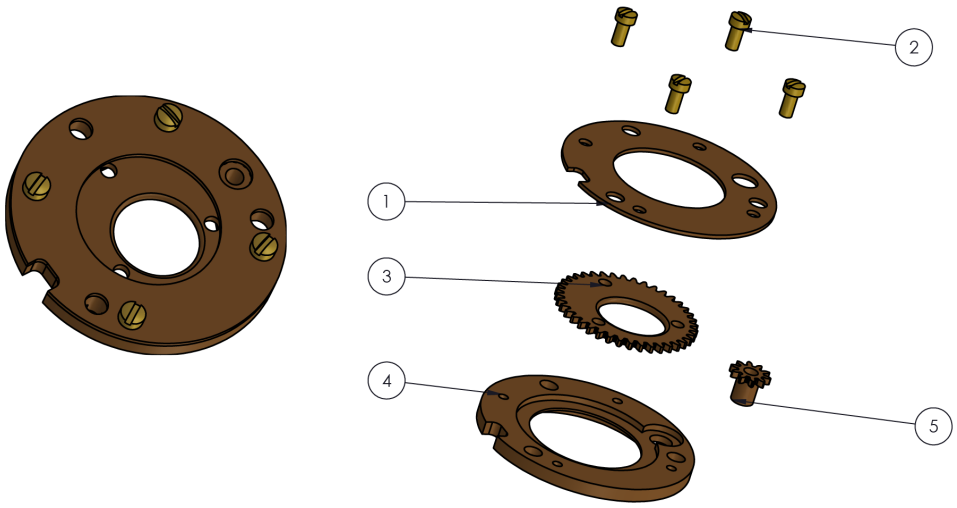

Figure 4.6: Drawing of the gear assembly. (1) is the top gear cover plate; (2) is the brass screw that holds the top gear cover plate to the gear cartridge (0-80 x .125"); (3) is the central ring gear that contains the aperture; (4) is the containing gear cartridge; (5) is the drive gear that interfaces between the control rod and the central ring gear.

not a good thermal conductor. The interfaces of the gear and cartridge surfaces are lubricated with Teflon spray to prevent friction from causing the mechanism to stick, which would result in loss of precision during the rotation.

The assembled probe components perform more than adequately in rotating the CB inside the control zone: we estimate to have control over the rotation of the carriage in steps of .125°, which is limited by the friction of the gear mechanism.[10]

Hysteresis Testing

It does not suffice to be able only to rotate the CB relative to the magnetic field, though: we must be able to ensure that it is parallel. Since the CB is at the far end of a long, hermetically-sealed tube this is not simply done, and so we have developed an indirect technique to measure the orientation of the resonator, informed by the results of a 2012 paper by Bothner, et al. [6]. The procedure makes use the 2G1P apparatus: the simple oscilloscope set-up.

Before presenting a summary of Bothner et al.'s conclusions, we recall some basic facts about the behavior of the resonance peak relative to the orientation of the resonator in the magnetic field. From the preceding theory regarding flux trapping, we understand that trapped magnetic flux

[10]We estimate this value by estimating the size of the "jumps" due to friction, measured in fractions of a rotation of the control rod. We can propagate these rotations along the rod and through the gear mechanism to get an estimate for the carriage rotation.

causes a degradation of the resonator's peak in terms both of reduced peak amplitude and of reduced resonance frequency. A certain amount of trapped flux is unavoidable in our experiment: after all, the resonator has finite width, and we only attempt to minimize, not eradicate, the resonator area projected normal to the magnetic field. Some lines will always penetrate the resonator. However, all else being equal an off-parallel resonator will trap more flux than one oriented parallel to the magnetic field, and thus the off-parallel resonator will exhibit a lower resonance frequency and diminished resonance peak amplitude. This degradation, if observed, is the smoking gun of misalignment.

We imagine a procedure to take advantage of this deterioration to align the resonator: first we locate the resonance peak at zero-field using the 2G1P apparatus, and afterwards we increase the field to some low level, say 100 Oe. We expect the peak to degrade slightly since it would trap flux (even if already perfectly aligned). After some short amount of time — on the order of seconds, as we observe experimentally — the peak will have reached an equilibrium at some lower resonance frequency and some peak amplitude. We then slightly rotate the control rod to effect a rotation of the resonator: the resonance peak must move again since it should have a different level of trapped flux. It will either have become better or worse aligned. If the peak degrades we know that the resonator has deviated further from parallel, and if the peak improves we know that it has moved closer to parallel. It is easy to envision how we could thus align the resonator by rotating the control rod in small increments and observing the effect on the oscilloscope: where the peak is sharpest and tallest is the frequency that corresponds with a parallel orientation.

Two issues prevent us from such a smooth execution: one mechanical, and one procedural. The first has to do with friction in the gear cartridge of the probe assembly: despite Teflon lubrication we often encounter significant friction in the rotation mechanism, such that the control rod "sticks". At these points we must apply a great deal of torque on the knob to match the static friction, and as soon as that is overcome the mechanism violently jumps. It is thus sometimes very difficult to apply small corrections to the rotation of the CB.[11]

The second issue is the one brought up by Bothner et al.'s study of magnetic hysteresis effects in superconductors. We reproduce two of their figures, Figs. 4.7 and 4.8, below as aids to explanation [6]. Figure 4.7 is a visual summary of what was discussed above: resonance peak degradation. (Although the increasing magnetic flux here is imposed by strengthening the magnetic field itself,

[11]This can be ameliorated somewhat if one understands the source of the friction. Referring back to Fig. 4.2, we see that the friction between the upper jack of the CB carriage and the central ring gear is greatest when the carriage is angled furthest away from the cable channel. This is due to the spring force of the cable loop below the carriage. If the parallel orientation of the carriage lies near this point, the sticking issue detailed in the main text becomes a very big problem indeed. There are two ways to attack the problem: we can either attempt to alter the optimal carriage orientation by biasing the mounting angle of the resonator on the CB appropriately; or we can lessen the spring force of the hook by deforming it slightly. We usually found the former method to produce sufficient results.

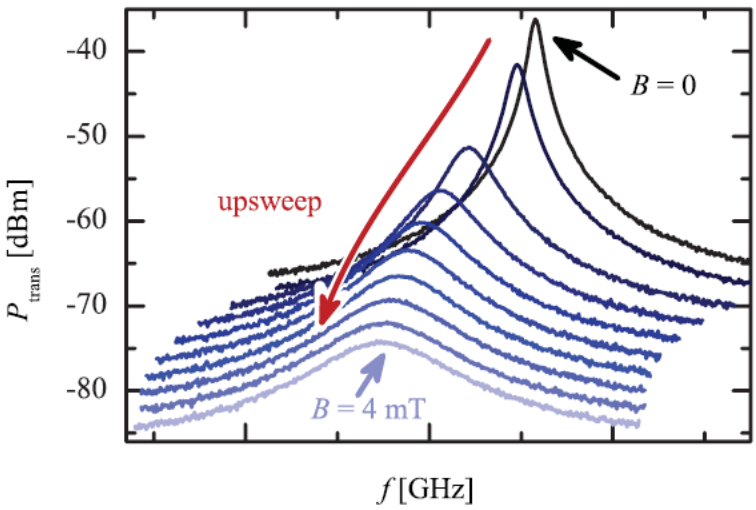

Figure 4.7: Resonance peak deterioration as a function of magnetic field. The $B = 0$ peak is sharpest and of highest resonance frequency, and the peak deteriorates both in terms of Q-factor and resonance frequency as the field is increased. Figure credit to Bothner et al. [6]

not changing the resonator's angle.) Figure 4.8 shows their results relevant to us, that the procedure we propose above is not entirely correct. Trapped magnetic flux will not entirely vacate the resonator even if zero-field conditions are restored. That is, once flux is trapped it cannot be purged except by bringing the superconductor above its critical temperature. So, during the above proposed test the peak may seem to be degraded despite the resonator actually being in a parallel orientation.

Working around this problem is simple but inefficient: we follow the alignment procedure as detailed above several times, each time making finer and finer adjustments, and in between each iteration we thermally cycle the PPMS.[12] The idea is that the hysteretic effects become less and less each iteration since we trap less and less flux each iteration, and thus we come very close to optimal orientation after several times through the procedure — 3 or 4 usually proves sufficient. We must repeat this procedure every time the probe is inserted into the PPMS as a precursor to any sort of measurement.

There also exists a more objective way of measuring the alignment of the resonator than merely eyeballing the movement of the peak on the oscilloscope screen, although that often turns out to be quite sufficient, as we may verify in the following manner. After having oriented the resonator to the best of our senses, we reconfigure to either the 2G2P or 3G apparatus to enable us to take precise measurements. We then produce a series of data like that in Fig. 4.8: we capture both a forward-sweeping and a backward-sweeping FvB curve. Overlaying the two should show a difference in

[12]Thermal cycling consists of warming the control zone to above the critical temperature of the resonator, then oscillating the magnetic field back to zero, and then cooling the control zone once again. This recreates the virgin conditions of the resonator and the magnet.

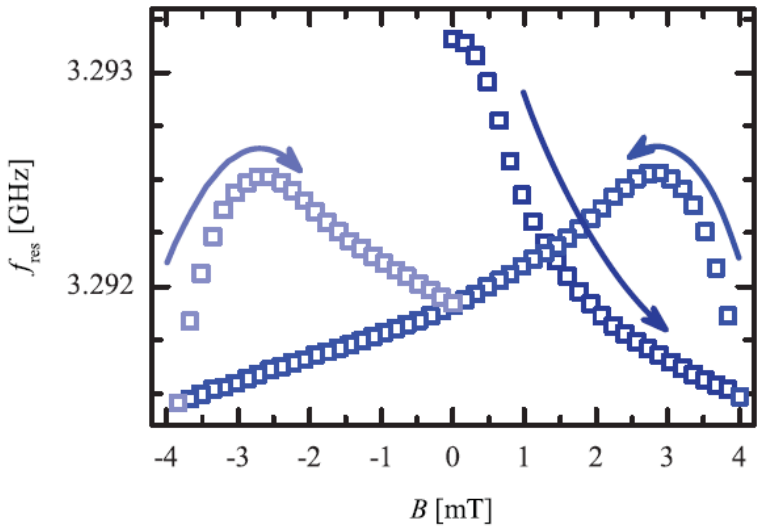

Figure 4.8: Effects of magnetic hysteresis on peak quality. The virgin state is represented by the square at zero-field with a resonance frequency of 3.932 GHz. The peak deteriorates (in terms of resonance frequency – a proxy for peak quality) as the field increases, but is not completely restored when the field is swept back. Figure credit to Bothner et al. [6]

frequency between the initial zero-field resonance and the final zero-field resonance: this difference being proportional to the amount of trapped flux. Thus, multiple orientations can be compared objectively on the basis of their zero-field separations. To illustrate the relative cases of poor and near-perfect orientation, we present the experimental results in Fig. 4.9. (Note that the estimated difference in angle between the resonator in these two measurements is only about .5 degrees.)

The above probe design and alignment procedure satisfactorily solve the issue we describe above in Chapter 3: as it stands we are able to consistently produce smooth FvB curves from a bare resonator, and so are well-equipped to search out sample spin interactions.

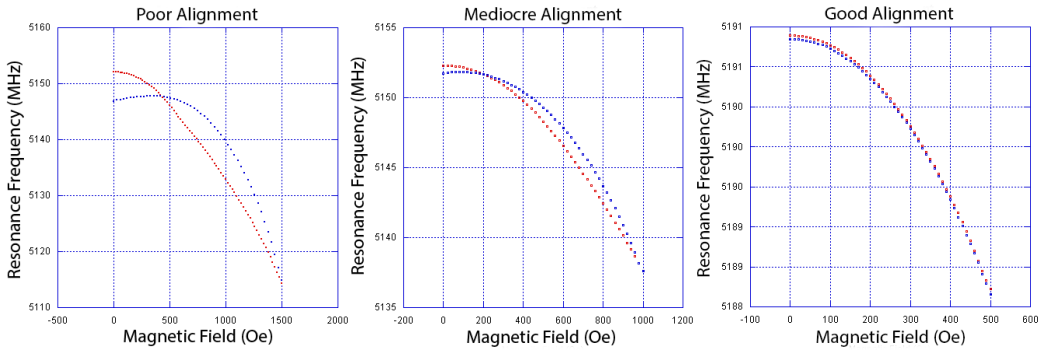

(a) (b) (c)

Figure 4.9: Comparison of resonator alignment's effects on hysteresis testing. (a) Shows the poorly aligned case, where the frequency difference at zero-field is great, and (c) shows the well aligned case, where the frequency at zero-field is small. (b) is a middle case. Note that the three sub-figures do not originate from similar power and temperature conditions.

Chapter 5

Results and Some Discussion

As of the time of writing, we have yet to observe any sample spin-resonator interactions, despite testing three SMMs: Cr_7Mn, Mn_3, and Ni_4. In lieu of presenting such results, then, we present characterizations of the niobium resonators: relationships between the resonance conditions and magnetic field, power, and temperature that were catalogued extensively in the search for interactions.

In the following discussions we will generically talk about resonance peaks, FvB curves, QvB curves, etc. with the understanding that they belong to the description of the bare superconducting resonator and not to the coupled system or the sample. Even in cases where the generated data actually comes from a coupled system, we are able to treat it as though it comes from an uncoupled resonator since the Hamiltonian for the coupled system is well approximated by the Hamiltonian for the uncoupled system

$$\hat{H} = \hat{H}_{\text{res}} + \hat{H}_{\text{spin}} - \vec{\mu} \cdot \vec{B} \rightarrow \hat{H}_{\text{res}} \tag{5.1}$$

except in cases of strong coupling. Because none of our data showed signs of strong coupling, this assumption is safe to make.

Magnetic Field Dependence

The behavior of the resonator in a variable magnetic field is the point of departure for all the work in this thesis, and so we present again a set of FvB and QvB curves, experimentally generated, in Fig. 5.1. These curves show what we have come to recognize as "good" behavior: they both have

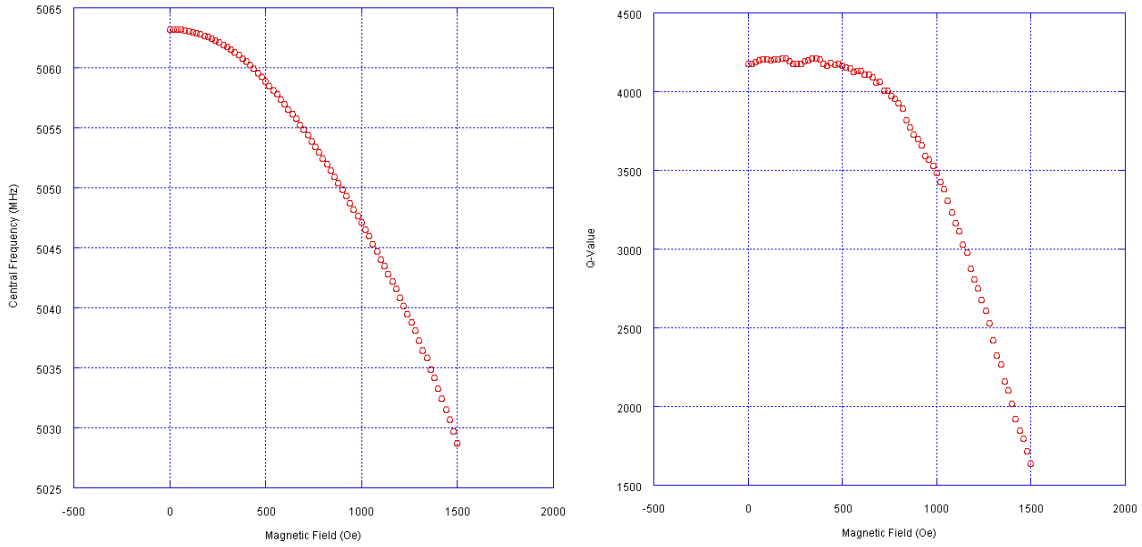

(a) (b)

Figure 5.1: Paired resonance frequency (a) and Q-factor (b) versus magnetic field plots, or FvB and QvB plots. This data was collected with the 2G apparatus at 2.4 K and -33dBm at the resonator.

negative curvature over the range of magnetic fields, which we attribute to magnetic flux trapping, and, apart from variations due to systematic noise,[1] there are no sharp features on either.

A sizable amount of time during this research was spent investigating the small features due to systematic noise, which primarily present themselves on the QvB plots. Initially we were unsure whether those features, one of which is seen at 300 Oe in Fig. 5.1b, were "real" or not, i.e. whether or not they were due to sample interaction. To answer this question we had to determine what was the size of a statistically significant feature for a given apparatus.[2] The question, then, is "What is the variance on the resonance frequency and quality factor measurements?" We can answer that question with the data in Fig. 5.2.

To estimate the variance on a measurement of, say, the resonance frequency of the resonator at 100 Oe and -33 dBm, we have only to take many traces of the resonance peak at these settings and then calculate the sample variance

$$\mathrm{Var} = \frac{1}{N}\sum_{i=1}^{N}(\nu_i - \bar{\nu})^2 \tag{5.2}$$

where ν_i is the particular observation of the resonance frequency and $\bar{\nu}$ is the sample average of all N observations of the resonance frequency. Since the sample variance is a consistent estimator,

[1] Most of the noise seems to come from the Lorentzian fitting process.

[2] The assumption here is that any noise seen is systematic and independent of conditions at the resonator, although we would expect the noise to scale with power.

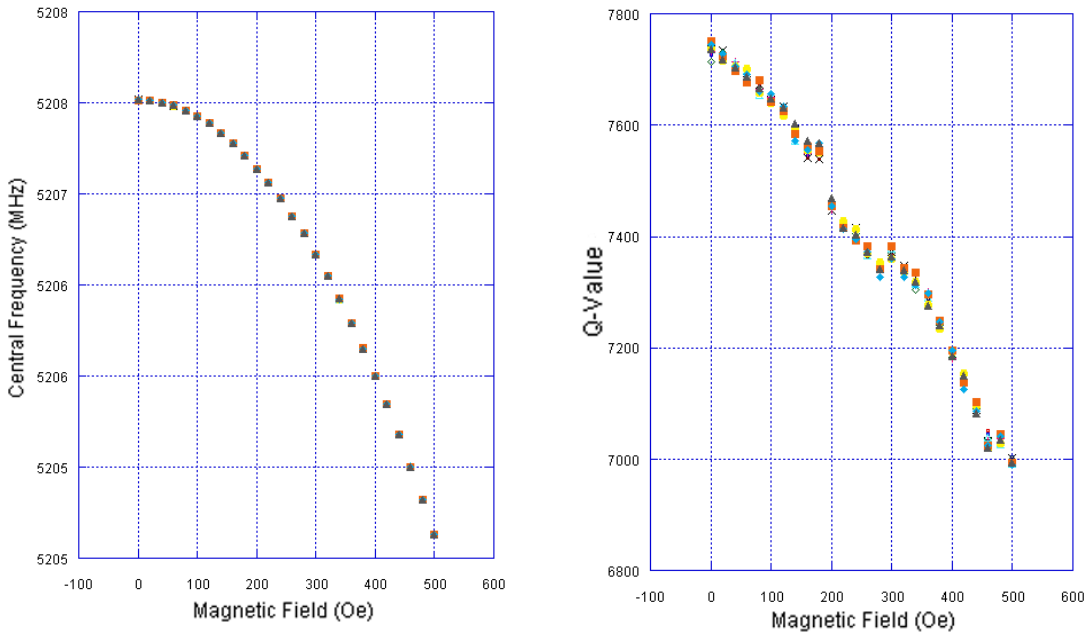

(a) (b)

Figure 5.2: Paired FvB (a) and QvB (b) plots. This data was taken by the 2G apparatus where we collected 10 resonance peaks at each magnetic field in sequence. The step in the QvB plot is a systematic artifact.

we would be content with the results of this calculation in the limit that N goes to ∞, but we are practically limited in the the number of trials we can make.

With some loss of accuracy we take $N = 10$ as sufficient, for the example given in Fig. 5.2. The particular experiment represented consisted of holding the magnetic field steady at one value while the frequency was swept across the resonance peak ten times in succession; then the field was increased and the process repeated. Each value of magnetic field was thus associated with ten traces, each of which was individually fitted to a Lorentzian curve the equation for which yielded the resonance frequency and quality factor parameters. Graphically, we immediately see that the noise in the Q-factor is an appreciable percentage of the total variation, whereas for the resonance frequency it is not. Thus, small features that we see in the QvB curve may very well be due to systematic noise.

More quantitatively, we see from Fig. 5.3 that the sample variance for the Q-factor averaged across all magnetic fields in Fig. 5.2b is 55.7, and that the sample variance for the resonance frequency averaged across all magnetic fields is 2.76×10^{-7} MHz^2. If we assume that the systematic noise is normally distributed, we can use the empirical rule to evaluate the likelihood that the feature in Fig. 5.1b is significant. That feature has a vertical scale of approximately ± 20, which is at the

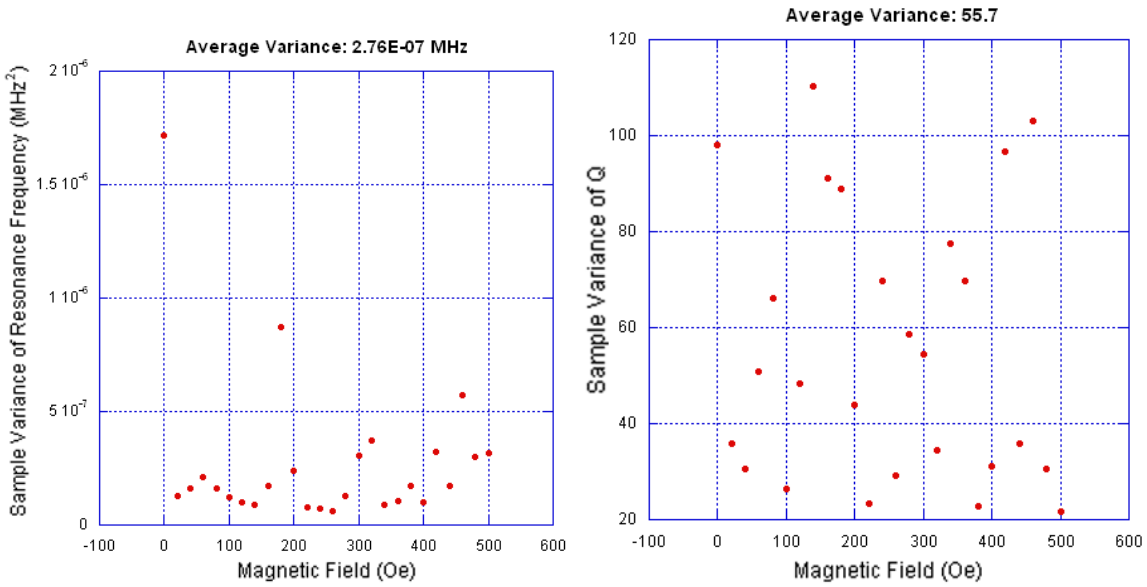

(a) (b)

Figure 5.3: Sample variance of resonance frequency (a) and quality factor (b) measurements.

$2-\sigma$ level. Thus we cannot be confident it is due to anything other than noise, although it may warrant further testing.

Temperature Dependence

The temperature dependence of the resonance peak, shown for the resonance frequency (Fig. 5.4) and for the Q-factor (Fig. 5.5), is nicely behaved and supports, at least qualitatively, the theory for Type II superconductors in Chapter 3.

The FvB curves in Fig. 5.4 show that the resonance frequency falls as temperature increases, and also that this dependence is independent of the applied magnetic field. We can explain this behavior as an increase in the resonator's kinetic inductance as the temperature approaches niobium's critical temperature: at higher temperatures there are fewer Cooper pairs in the material to form the electric current. Since the resonance frequency of the resonator can be approximated as that of an RLC circuit, $\omega_0 = 1/\sqrt{LC}$, an increase in inductance (of which kinetic inductance is a constituent) lowers the resonance frequency.

The QvB temperature dependence in Fig. 5.5 is similar: the Q-factor decreases with increasing temperature. This effect can be ascribed to an increasing *effective* resistance in the resonator. Using again the RLC approximation, Q-factor$= (\omega_0 L)/R = \sqrt{L}/(R\sqrt{C})$, we see the increasing resistance must overpower the increasing inductance. Both the resonance frequency and Q-factor effects can

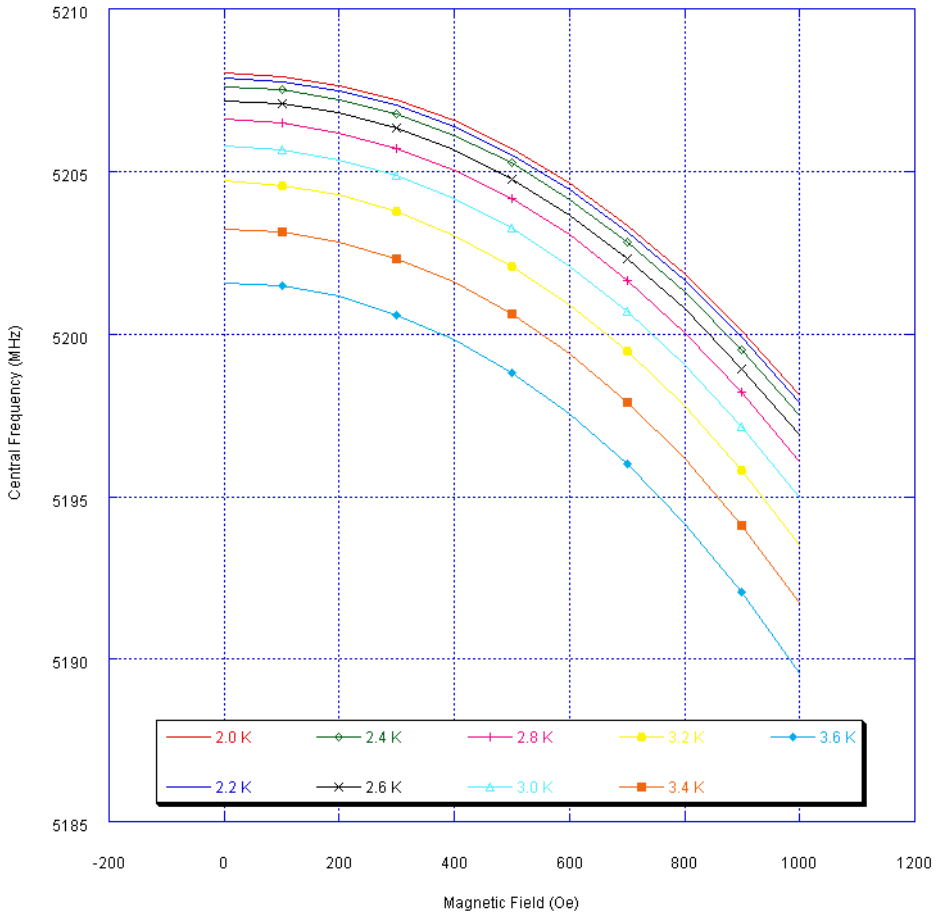

Figure 5.4: Resonator behavior by temperature. The resonance frequency is shown for various operating temperatures as a function of applied magnetic field. These tests were conducted by the 2G apparatus at -33 dBm at the resonator.

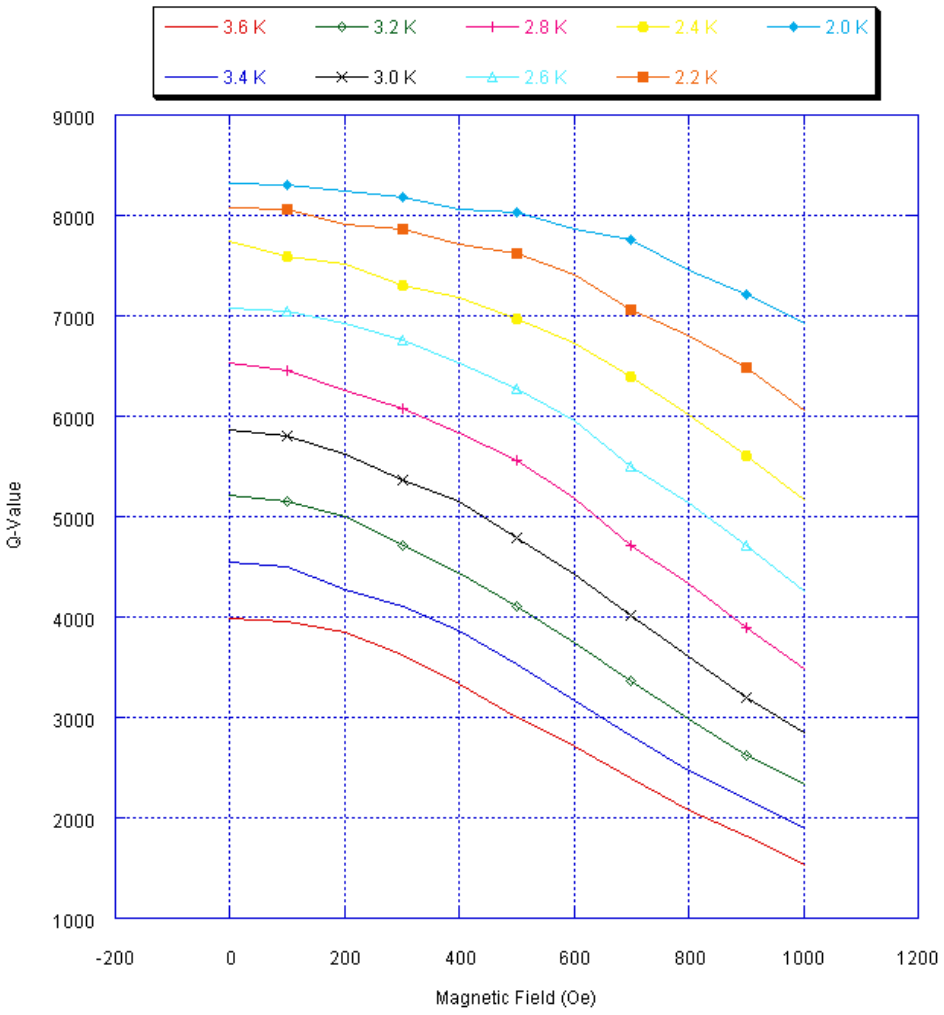

Figure 5.5: Resonator behavior by temperature. The resonance quality factor is shown for various operating temperatures as a function of applied magnetic field. These tests were conducted by the 2G apparatus at -33 dBm at the resonator.

be visualized together with a progression of peaks, as in Fig. 5.6.

The combination of these results suggests, as we could have predicted, that we want to operate our resonators at the lowest temperature possible to benefit from higher Q-factors and signal-to-noise ratios.

Power Dependence

A first glance at the FvB dependence on power, shown in Fig. 5.7, might conclude that there is no discernible effect. A closer look in Fig. 5.8, however, reveals that higher powers seem to depress the resonance frequency. Fig. 5.9 gives another point of view on the effect: we see that at higher

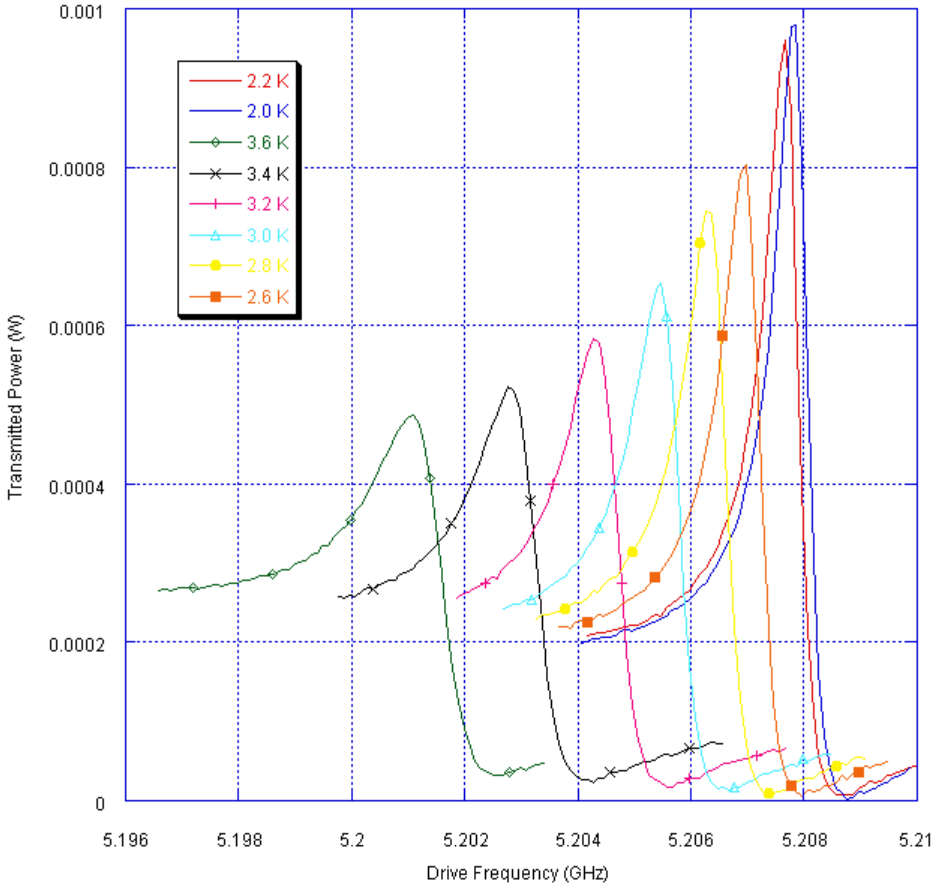

Figure 5.6: Resonance peak shape as a function of temperature. Notice that the peak amplitude falls off similarly to resonance frequency at increasing temperatures. Each curve was taken by the 2G apparatus at 100 Oe applied field and -33 dBm at the resonator. (Note the skewed Lorentzian shapes that result from measuring the untransformed magnitude of the transmitted power. Magnitudes measured with the 3G apparatus, like those in Fig. 5.9, are much better behaved.)

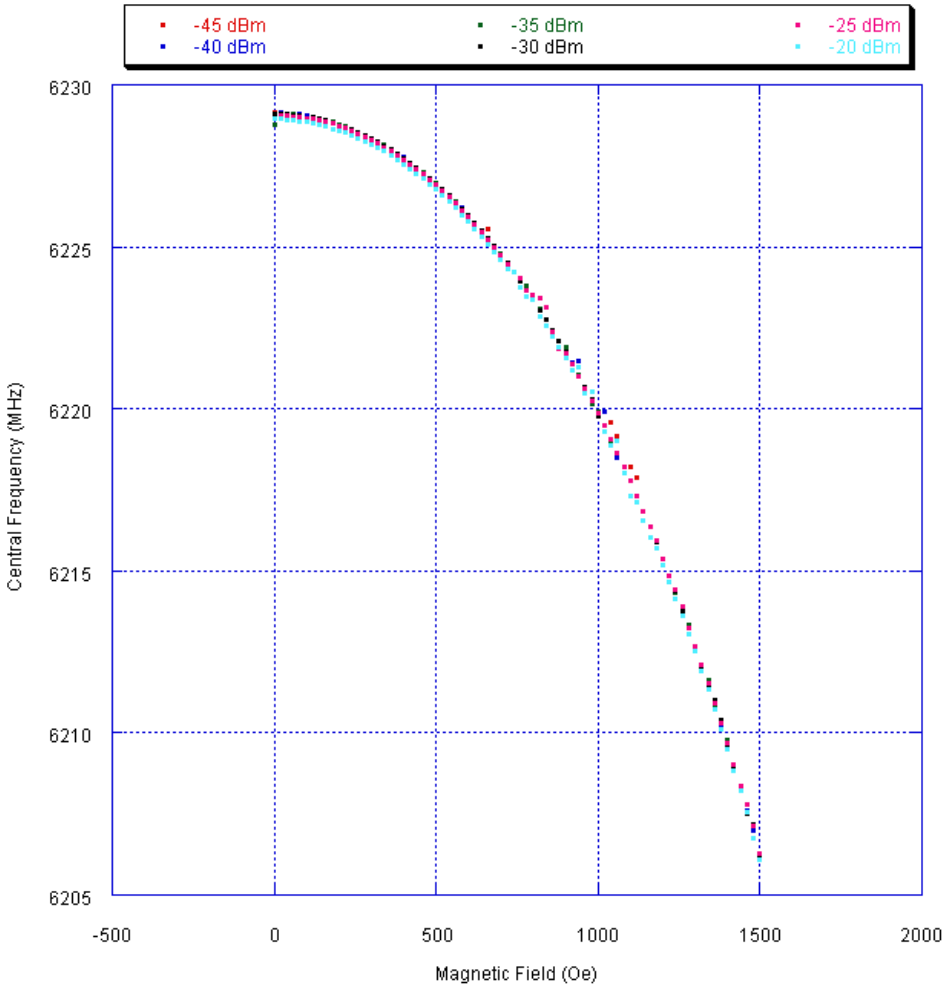

Figure 5.7: Resonator behavior by RF power, as measured by the 3G apparatus. Each curve was taken at 1.8 K.

powers the peaks are "leaning into" the frequency sweep (swept low to high), i.e. the leading slope is much steeper than the trailing slope. This behavior, which matches that found by Snortland [24], is due to increasing kinetic inductance at higher powers.

Kinetic inductance refers to the inertial lag that charge carriers, like all particles with non-zero mass, experience during acceleration. The acceleration in a high frequency resonator naturally leads to high kinetic inductance. The effect that kinetic inductance has on a circuit element is indistinguishable from that caused by the magnetic inductance, so that the total inductance L is just $L_m + L_{ki}$. [11]. We can understand this effect heuristically according to the concept of a critical current that we developed in Chapter 3: as the current increases, so too does the kinetic inductance of the resonator. Then because increased inductance causes the resonance frequency to degrade, and because current in the resonator increases near the resonance frequency, the resonance frequency

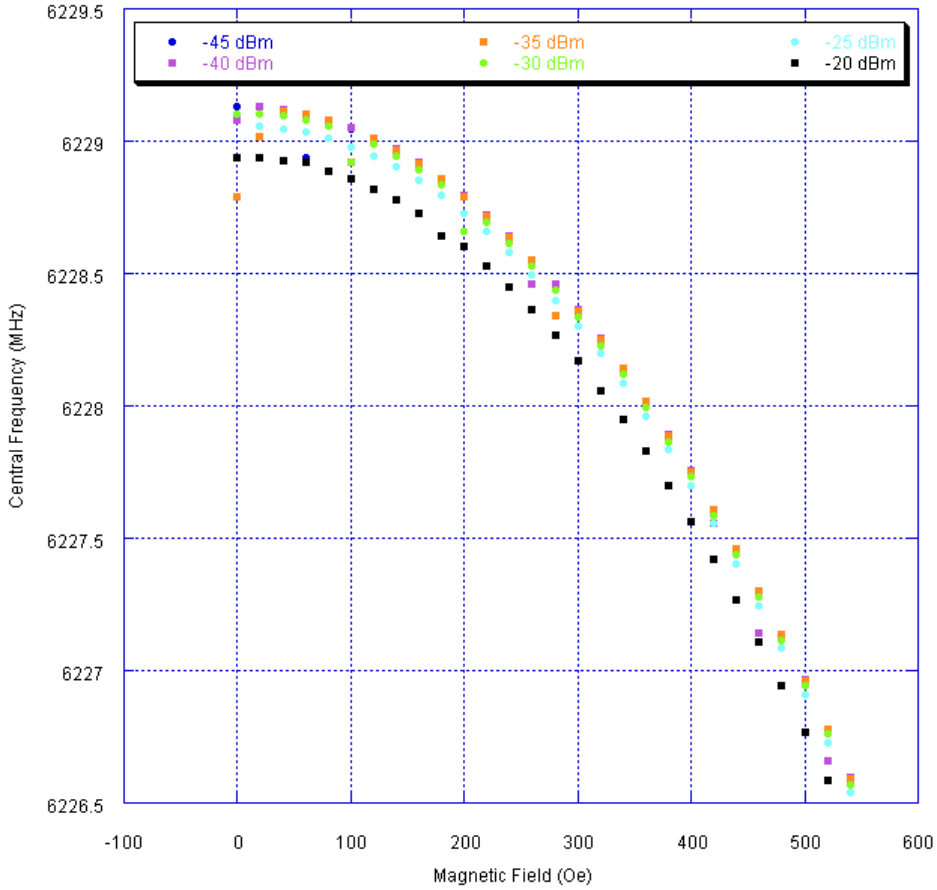

Figure 5.8: Magnified resonator behavior by RF power, as measured by the 3G apparatus. Here we are able to see the effect of kinetic inductance. Each curve was taken at 1.8 K.

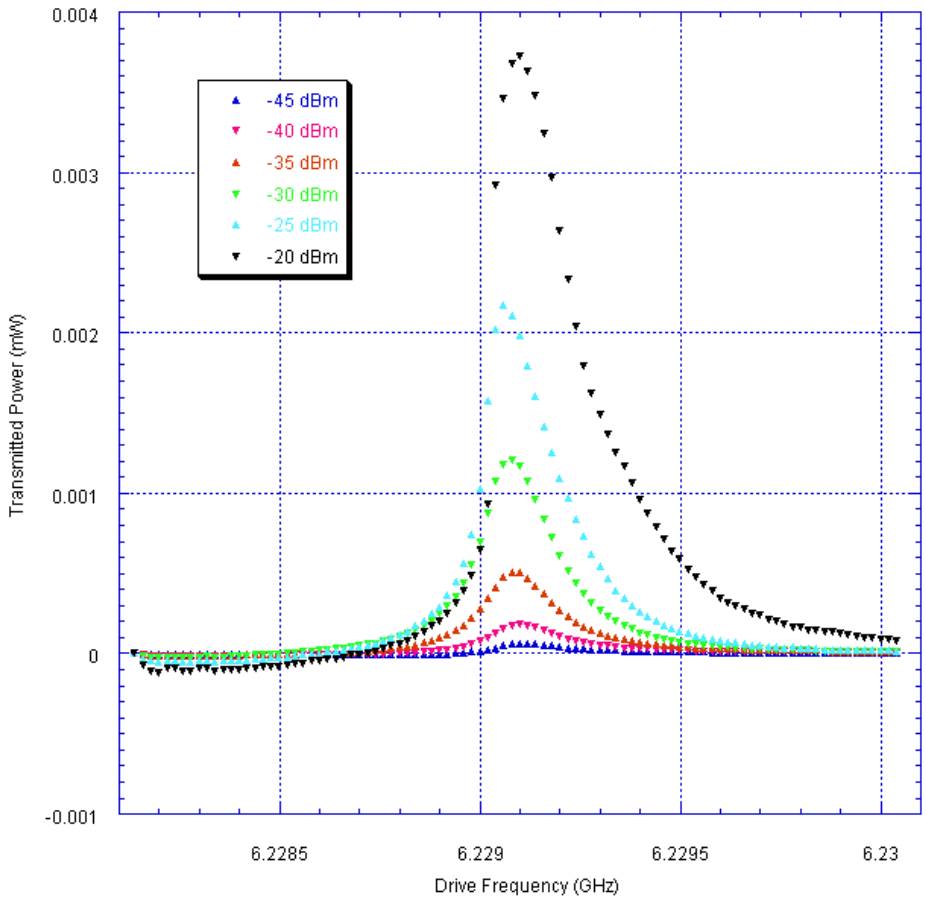

Figure 5.9: Resonance peak shape as a function of RF power. We see that not only are higher power curves taller and wider, but their leading slope is also steeper than their trailing slope. Low power peaks do not display such asymmetry. Each curve was taken by the 3G apparatus at 100 Oe applied field and 1.8 K.

falls even as it is approached from below. For low power in the resonator, this effect is negligible, as is evidenced by the symmetric -45 dBm curve in Fig. 5.9; for high powers, though, we see a real effect, as shown by the highly asymmetric -20 dBm curve in the same figure.

Conclusions

The original goal of this research — the characterization of the magnetic properties of a handful of single molecule magnets — remains ahead of us, despite nearly a year of progress for the apparatus and procedures necessary to perform the characterization. After every iteration of the probe, the measurement system, and the data analysis software, we had renewed hope of observing interaction between an SMM sample and the resonator, but we have yet to observe anything. Why? We seem

to recycle theories as quickly as we go through apparatus configurations.

The first theory, that the sample-resonator interaction was being obscured by poor resonator performance due to magnetic flux trapping, was discredited after construction of the adjustable probe. We are now able to consistently produce high quality FvB curves for the resonator that indicate it has fine working performance at the magnetic fields where we expect strong coupling with the samples.

A second theory, that we were losing the interactions in the noise of the FvB and QvB plots, became less and less plausible as every new iteration of our methods brought better and better signal-to-noise ratios. Recalling the result earlier in this chapter that the standard deviation of a resonance frequency measurement due to systematic noise is around 500 Hz,[3] it becomes difficult to believe that we might completely miss the signs of an interaction.

A third theory, which we are still testing, is the possibility that the power of the RF signal we are coupling with the SMMs is actually causing the sample to saturate; i.e., for the relevant energy transition we are exciting states faster than they relax, and so there is no net power absorption to see. Initial calculations in the limit of $n_{\text{photons}} \gg n_{\text{spins}}$ indicated that we should not experience saturation at our normal operating power of roughly -35 dBm at the resonator. Given the excellent signal-to-noise ratio of the 3G apparatus, we have been able to test this theory by further decreasing the RF signal power to -45 dBm at the resonator, increasing the margin on our estimation considerably. Still we have had no success. Rather than continue trying to operate with sustained low powers, it may make sense in the future to attempt pulsed ESR experiments.

A final and seemingly desperate theory — although the alternatives do to us seem exhausted — is that the samples themselves are problematic. Thanks to fruitful collaborations, however, we hope to have new samples in our possession soon, and we hope that they will provide us with more success.

In the meantime, the trajectory of the research continues as we find new ways to improve the apparatus. A particularly elusive technical issue is the skew to the Lorentzian curves that we fit to the magnitude of the transmitted power, and likewise the ellipses we get from the 3G apparatus when we expect circles. This issue only appeared after introducing the new probe into the system, and thus a prime suspect for the effect is impedance mismatching caused by the stress on cable connections due to the circuit board rotations. Although the benefits of the newer apparatuses undoubtedly outweigh this annoyance, there seems to be no reason that further creativity cannot also purge it from the apparatus.

[3] Std. Dev. $= \sqrt{\text{Var}} = \sqrt{2.76 \times 10^{-7}\ \text{MHz}^2} \approx 516$ Hz.

Appendix A

Signal Flow Analysis[1]

Signal flow theory, or transmission line theory, describes the propagation of electromagnetic waves along transmission lines, specifically for the case where the wavelength of the signal is short compared to the circuit.[2] This case definitely applies for the signals we use, on the order of 5 GHz, corresponding to $\lambda = c/f \approx .1$ m compared to an overall circuit length more than ten times as long.

For the purposes of this research we are interested in examining what happens to the signal, output by the microwave generator, as it passes through the circuit including the resonator, and is ultimately measured in some way by our apparatus.

We can represent any network schematically with the "black box" model shown in Figure A.1, where V_n+ is a measure of signal incident on Port 1, and V_n- is a measure of reflected signal leaving Port n. The black box contains all of the circuitry intervening between the ports. The input and output measurements of the circuits can be related with the scattering matrix S:

$$\begin{pmatrix} V_1- \\ V_2- \\ \vdots \\ V_n- \end{pmatrix} = \begin{pmatrix} S_{1,1} & S_{1,2} & \cdots & S_{1,n} \\ S_{2,1} & S_{2,2} & \cdots & S_{2,n} \\ \vdots & \vdots & \ddots & \vdots \\ S_{m,1} & S_{m,2} & \cdots & S_{m,n} \end{pmatrix} \begin{pmatrix} V_1+ \\ V_2+ \\ \vdots \\ V_n+ \end{pmatrix} \tag{A.1}$$

The scattering matrix represents the effects of the elements in the black box. Recall from Figure 2.9 the complex transformation that the resonator applies to an incident wave; in general, we can say that any circuit element will similarly impose both magnitude and phase transformations on an incident signal. This complex transformation is what the scattering matrix represents. In our case

[1] The following is largely informed by David Pozar's excellent *Microwave Engineering* [21], and the reader is referred there for more information on the topic.

[2] Thus we do not need transmission line theory to explain household circuitry, with the low frequencies of 60 Hz.

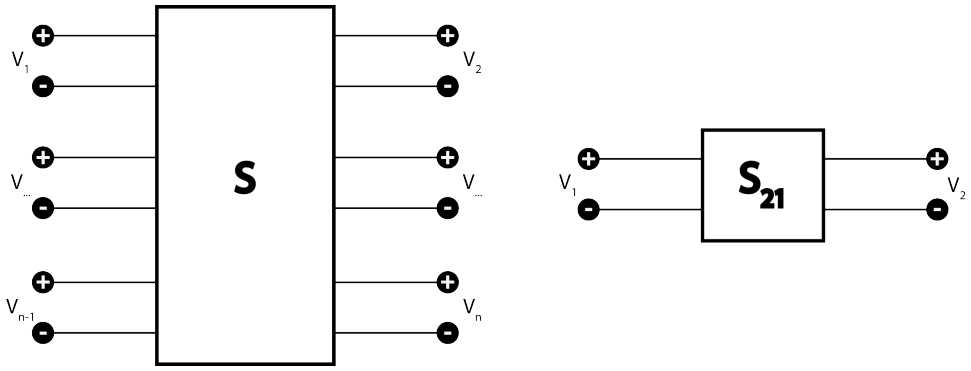

Figure A.1: Schematics of a general n-port network as a "black box" model, and a general 2-port network. The "S" represents the transformation imposed by the circuit.

it will prove quite sufficient to restrict ourselves to a two-port network using the equation

$$S_{2,1} = \frac{V_2-}{V_1+}. \tag{A.2}$$

and so avoiding the large scattering matrix of Eq. A.1. This is entirely appropriate both for the 2G apparatus, where the signal is produced at the RF generator and is measured at the lock-in, and for the 3G apparatus, where the signal is produced at the RF generator and is measured at the mixer.

Working with the black box model, and using the network analysis from Howard Snortland's 1997 dissertation [24], we can populate the box in Fig. A.1 with the generic circuit elements of our 3G network in Fig. A.2 (a). These elements are an amplifier, a transmission line, the resonator, and parallel parasitic resonances. It is intuitive to see how we might break up this one black box into a combination of in-series and in-parallel black boxes, each having its own scattering matrix, as in part (b) of the same Figure. Indeed, signal flow theory supports this intuition.

It is also intuitive, and fundamental to signal flow theory, that we can re-combine these separate scattering matrices back into the one scattering matrix by a set of 4 simple rules:[3]

$$V_2- = S_{2,1}V_1+ \text{ or } V_{\text{out}} = S_{2,1}V_{\text{in}}. \tag{A.3}$$

Snortland has performed this combination for the case in Fig. A.2, yielding

$$S_{2,1} = \frac{(1-\Gamma_{\text{in}})(1-\Gamma_{\text{out}})\Theta}{1-\Theta^2\Gamma_{\text{in}}\Gamma_{\text{out}}}(S_{\text{res}} + S_{\text{par}}), \tag{A.4}$$

where Θ relates to the propagation along the transmission line, Γ_{in} and Γ_{out} relate to reflection on the ends of the transmission line, S_{res} corresponds to the scattering of the resonator, and S_{par}

[3]The series, parallel, self-loop, and splitting rules. See Pozar, p. 214 for more details [21].

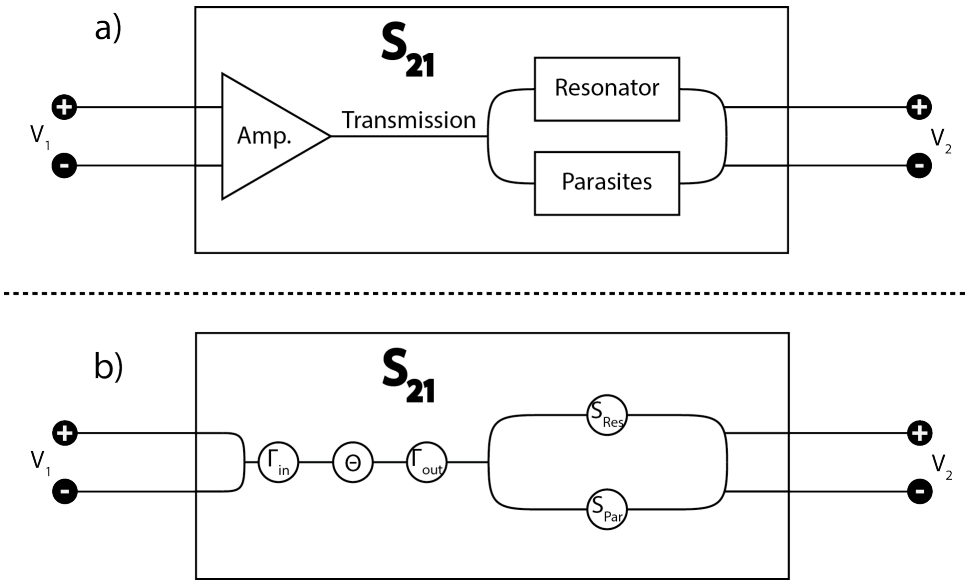

Figure A.2: A "black box" schematic of our network, consisting of amplifier, transmission line, resonator, and parasitics. The figure credit goes largely to Howard Snortland.

corresponds to the scattering of any parasitic resonances. The term $S_{2,1}$, then, encapsulates all of the transformations that occur to the original signal output by the microwave generator before it is measured by us. In theory, we have only to multiply the known input signal by $S_{2,1}$ to retrieve the output signal that we measure.

Fitting Procedure[4]

Examining the above equation in the context of our different apparatuses, we see that the 1G and 2G apparatuses only measure the magnitude of $S_{2,1}V_{\text{in}}$ (since those apparatuses rely on the power diode), and the 3G apparatus measures both the magnitude and phase[5] of $S_{2,1}V_{\text{in}}$. The magnitude and phase data we are already well acquainted with, but not the complex data that the IQ mixer in the 3G apparatus outputs. This data is in the form of complex pairs $z = x + iy$, and can be plotted as an ellipse in the complex plane, as in Fig. A.3.[6] Using simple trigonometry we can reconstruct the magnitude data with

$$\text{Magnitude} = \sqrt{x^2 + y^2}, \tag{A.5}$$

and the relative phase information with

[4]This section draws from Snortland's [24], Ma's [18], and Gao's [12] works.
[5]By phase here we mean the relative phase between V_{out} and V_{in}.
[6]The referenced articles and dissertations refer to the data being ideally shaped as a circle. Snortland mentions that an elliptical shape is due to a nonlinear response in resistivity [24].

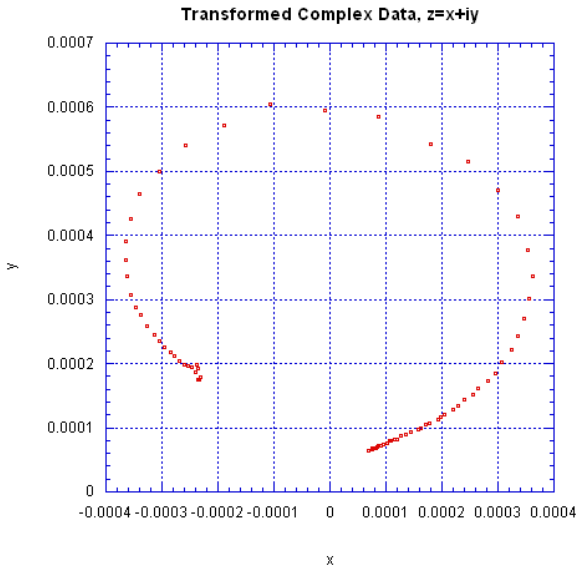

Figure A.3: Complex data in the form of an ellipse.

$$\text{Phase} = \arctan \frac{y}{x}. \tag{A.6}$$

We would expect the reconstructed magnitude data from a 3G measurement to match the magnitude data from a 2G measurement (perhaps with some slight disagreement due to the different methods of measurement) since they both measure the same $S_{2,1}V_{\text{in}}$ signal.

But the complete phase and magnitude information obtained by the 3G apparatus has more potential. Notice that Eq. A.4 consists of a prefactor

$$\frac{(1-\Gamma_{\text{in}})(1-\Gamma_{\text{out}})\Theta}{1-\Theta^2\Gamma_{\text{in}}\Gamma_{\text{out}}}, \tag{A.7}$$

and a resonance factor

$$(S_{\text{res}} + S_{\text{par}}). \tag{A.8}$$

We really are interested only in the S_{Res} term, since that is the complex transformation due to the resonator and any sample that may be mounted to it; the other terms constitute unwanted noise.[7]

[7]It so happens that the S_{Res} term dominates close to resonance, and so the 2G2P apparatus is justified as a reliable, if relatively imprecise, stand-in for the 3G apparatus. The undesirable noise is easy to see, though, in the background of Fig. 2.5, for example.

The complete complex data allows us to extract that term through data transformations.

In general, multiplying one complex number by another transforms the first by scaling and rotating it, while summing two complex numbers results in a translation. Given the equality of the measured data, V_{out}, and the transformed input, $S_{2,1}V_{\text{in}}$

$$V_{\text{out}} = S_{2,1}V_{\text{in}}, \tag{A.9}$$

we can remove the prefactor by rotating and scaling the complex V_{out} data,

$$(\text{rotation})V_{\text{out}} = (S_{\text{res}} + S_{\text{par}})V_{\text{in}}, \tag{A.10}$$

and we can remove the S_{par} term by translating the V_{out} data,

$$(\text{rotation})V_{\text{out}} - (\text{translation}) = S_{\text{res}}V_{\text{in}}, \tag{A.11}$$

the holy grail.

Creating a magnitude and a phase plot from the transformed $S_{2,1}V_{\text{in}}$ data should yield more accurate measurements of the resonator quality factor and resonance frequency, and that is precisely the progress we made by designing the 3G apparatus.

Details on the Ellipse Fitting Process

We now provide the details of transforming the raw V_{out} data into the desired $S_{\text{res}}V_{\text{in}}$ form.

The problem is just to rotate and translate a general ellipse such that it lies along the real axis, extending away from the origin. We know this from classical resonance theory, and we showed it for the magnitude and phase individually in Figs. 2.10a and 2.10b: the phase should complete a full π change, and the magnitude should peak at resonance. These conditions are satisfied for the mentioned position and orientation.

The initial form of the data is a general ellipse described by the equation

$$\frac{\left((x - x_0)\cos\theta + (y - y_0)\sin\theta\right)^2}{a^2} + \frac{\left((x - x_0)\sin\theta - (y - y_0)\cos\theta\right)^2}{b^2} = 1, \tag{A.12}$$

where the complex pairs $z = x + iy$ represent the raw data, the pair $z_0 = x_0 + iy_0$ is the center, and θ is the degree of rotation. The final (desired) form of the transformed data is the canonical ellipse

$$\frac{x^2}{a^2} + \frac{y^2}{b^2} = 1. \tag{A.13}$$

So we set up the transformation:

$$z_c \text{ (corrected z)} = (z_0 - z) * e^{-i\theta}, \tag{A.14}$$

or in component form:

$$(x_c + iy_c) = ((x_0 + iy_0) - (x + iy))(\cos(-\theta) + i\sin\theta). \tag{A.15}$$

This can be broken into and simplified as

$$\begin{aligned} x_c &= (x_0 - x)\cos\theta + (y_0 - y)\sin\theta \\ y_c &= (y_0 - y)\cos\theta - (x_0 - x)\sin\theta \end{aligned} \tag{A.16}$$

To apply these transformations, it only remains to acquire the parameters z, z_0, and θ by fitting the original raw data to the general ellipse of form Eq. A.12. The accurate magnitude and phase plots can then be generated from z_c.

Fitting the Magnitude and Phase Plots[8]

A more analytically rigorous approach to the derivation of Eq. A.11 is carried out by Ma [18], and his result may be shown to give

$$S_{2,1} = \frac{2\omega^2 l_{m1} l_{m2}/Z_0 L}{R/2L + i(\omega - \omega_0)} \tag{A.17}$$

where Z_0 is an impedance characteristic to the transmission cables, the l_m terms are characteristic of the coupling inductance between the resonator and rest of the circuit, R and L are the equivalent resistance and equivalent inductance of the resonator as modeled by a series LCR circuit, and ω_0 is the resonance frequency.

We can simplify this equation by noting that the resonance frequency of an LCR circuit is

$$\omega_0 = \frac{1}{\sqrt{LC}}, \tag{A.18}$$

[8]This section is informed by Petersan [20], Gao [12], and Taylor [25].

and that the Q-factor is

$$Q = \frac{\omega_0}{\text{FWHM}} = \frac{\omega_0}{R/L} = \frac{\sqrt{L}}{R\sqrt{C}}. \tag{A.19}$$

Also we see that at resonance, where $\omega = \omega_0$, that

$$S_{2,1}(\omega = \omega_0) = \frac{4\omega^2 l_{m1} l_{m2}}{Z_0 R}, \tag{A.20}$$

which we denote as $S_{\max}$.

We can then rewrite

$$\begin{aligned} S_{2,1} &= \frac{S_{\max}}{1 + iQ(\frac{\omega^2 - \omega_0^2}{\omega\omega_0})} \\ &= \frac{S_{\max}}{1 + 2iQ(\frac{\omega - \omega_0}{\omega_0})} \end{aligned} \tag{A.21}$$

near resonance.[9] Thus we have found an explicit form for the scattering element $S_{2,1}$. Multiplied by the known input signal, this provides us with the expected form for the output signal.

From Eq. A.21 we can extract both the magnitude and phase behavior. The magnitude squared is

$$|S_{2,1}|^2 = \frac{|S_{\max}|^2}{1 + 4Q^2(\frac{\omega - \omega_0}{\omega_0})^2}, \tag{A.22}$$

which we recognize as a Lorentzian. Since it is a function of both the resonance frequency and the Q-factor, we can extract the two parameters from data fitted with this equation. Because we often deal with background signal superimposed on our resonance peaks, and because we deviate from ideal resonance behavior due to (we theorize) mismatched impedances, we add in extra terms to form the more robust skewed Lorentzian:

$$|S_{2,1}|^2 = A_1 + A_2(\omega - \omega_0) + \frac{A_3 + A_4(\omega - \omega_0)}{1 + 4Q^2(\frac{\omega - \omega_0}{\omega_0})^2}. \tag{A.23}$$

Fitting to this curve instead yields more accurate estimates for the resonance frequency and the Q-factor.

The phase can similarly be found:

[9] Near resonance $\omega \approx \omega_0$, so $\frac{\omega^2 - \omega_0^2}{\omega\omega_0} = \frac{(\omega + \omega_0)(\omega - \omega_0)}{\omega\omega_0} \implies \frac{(2\omega)(\omega - \omega_0)}{\omega\omega_0}$.

$$\phi = 2\arctan\left(2Q \cdot \frac{\omega_0 - \omega}{\omega_0}\right) + \phi_0 \tag{A.24}$$

where ϕ_0 is a constant originating from the transmission line phase delay (a constant phase factor on Eq. A.17) [18]. For a resonator with a reasonably high Q-factor (on the order of 10^4 or higher), the arctangent very quickly flips from $-\pi/2$ to $\pi/2$ where the resonance frequency is where the curve crosses 0. For these resonators the phase plot is a very precise way of determining the resonance frequency.

Appendix B

Predicting Sample Interaction and the Giant Spin Approximation

The interaction between sample spins and the superconducting resonator occurs at the drive frequency and bias magnetic field combination that satisfies both systems' resonance conditions. Because we typically characterize our resonators with curves on a frequency vs. magnetic field plot, and because the sample's resonance condition can be characterized the same way — a relationship between frequency and bias field at resonance — the question of finding the "interaction location" comes down to finding the point at which these curves intersect. The resonator's FvB curve is experimentally determined, and that process has been described at length in the main text body.[1] The determination of the sample's FvB curve is described here.

The sample's resonance frequency is the frequency, generally magnetic field dependent, that corresponds to the energy difference between the two energy eigenstates of interest:

$$\Delta E = \hbar\omega(B) \tag{B.1}$$

So to find this frequency it suffices to find the energies of the two states in which we are interested, and we do this just by finding the eigensystem of the relevant Hamiltonian.

The samples that we work with, single molecule magnets (SMMs), are composed of clusters of paramagnetic transition metal ions in a diamagnetic lattice. To accurately characterize the energies of this system requires accounting not only for each ion's interaction with the crystal field but also each ion's interaction with all other ions. Separating out the unpaired electrons of the ions as our

[1] Mainly in Chapter 2 Section 2.

spins of interest and considering their interactions can give a seemingly uncountable dimensionality: an SMM like Mn_{12},[2] (admittedly a large molecule) has a Hilbert space with 10^8 dimensions, which is not feasible to work with [29].

The Giant Spin Approximation (GSA) makes calculations more practical by dramatically reducing the Hilbert space dimensionality. Ni_4, for instance, is composed at its core of four spin-1 Ni^{2+} ions, and, restricting our consideration only to this core, then has a Hilbert space spanning 81 dimensions.[3] The GSA combines these four separate spins into one "giant" spin-4 system with only 9 dimensions — a very tractable number. The next step, constructing the resulting Giant Spin Hamiltonian only takes into account intrinsic spin contributions and the symmetry of the molecule (which is determined by the crystal potential, itself an approximation of the spin-lattice interactions).[4]

The GS Hamiltonian consists of a term grouping to account for zero-field spin-spin interactions and a term grouping to account for the field dependent Zeeman interactions:[5]

$$\hat{H} = \mathbf{S} \cdot \tilde{\mathbf{D}} \cdot \mathbf{S} + \mu_B \mathbf{B} \cdot \tilde{\mathbf{g}} \cdot \mathbf{S}, \tag{B.2}$$

where $\tilde{\mathbf{D}}$ is a tensor regulating the interaction between the $\mathbf{S}$ combined spin operators, and $\tilde{\mathbf{g}}$ is the Landé g-factor, which plays a similar role between the external magnetic field $\mathbf{B}$ and the combined spin operator.

We first simplify the second term grouping: the g-factor takes a tensor form since, in general, the Zeeman interaction depends not only on the relative orientation of $\hat{S}_n$ and $\mathbf{B}$, but also on the orientation between $\mathbf{B}$ and other symmetry-dependent axes in the molecule. With a few assumptions,[6] we approximate the g-factor to a scalar value, and we can rewrite

$$\mathbf{B} \cdot \mathbf{S} \implies B\hat{S}_n \tag{B.3}$$

where $\hat{S}_n$ is just the projection of the spin operator in the direction of the external magnetic field.

The first term grouping devolves differently according to the specific symmetries of the molecule. It is in general a series of Stevens operators expanded as spherical harmonics, but the allowed terms depend upon the specific system and its anisotropies. A spherically symmetric molecule,

[2] $Mn_{12}O_{12}(O_2CCH_3)_{16}(H_2O)_4$

[3] A single $S = 1$ spin has $2S + 1 = 3$ dimensions, so four $S = 1$ spins have $3^4 = 81$ dimensions.

[4] In recent years a number of articles have been published concerning the appropriateness of the GSA for research; conclusions have been that while the Giant Spin Hamiltonian does perform adequately in predicting behavior, the coefficients (experimentally determined) that belong to that Hamiltonian are convolutions of many physical effects, and so the GSA is not necessarily appropriate for explanatory models [29] [17].

[5] We only sketch the derivation of the GS Hamiltonian here, but direct the reader to Lawrence [17] for further explanation.

[6] See Abragam pp. 14-16 [1] for more details.

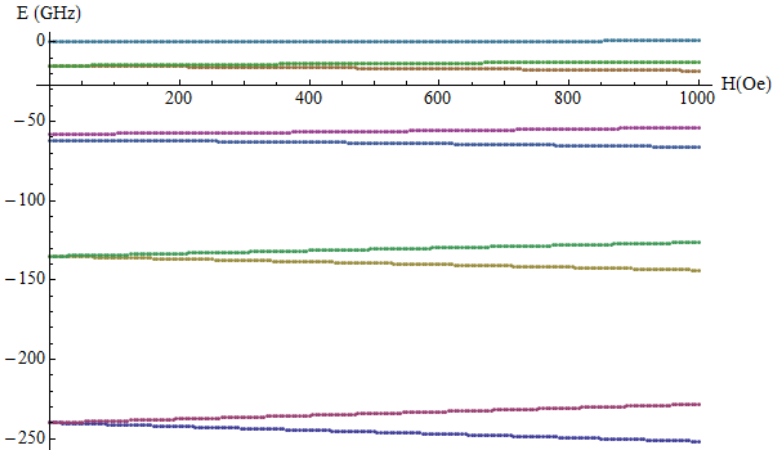

Figure B.1: Energy Eigenvalues of Ni_4 by Magnetic Field (under the Giant Spin Approximation).

for example, would include no anisotropic terms since it is by definition isotropic. A cubically symmetrical molecule would contain anisotropic terms, specifically of the fourth order. What is common to all SMMs under the GSA is the presence of a $D\hat{S}_z^2$ term, which represents a large axial anisotropy that, given D negative, biases the magnetization of the molecule in either of two directions, which define the "easy axis" of the sample.

For the rest of this section, we will take as an example Ni_4, which is cubically symmetric with S= 4, and so the correct GSA Hamiltonian is given by [7]

$$\hat{H} = D\hat{S}_z^2 - B\hat{S}_z^4 + C(\hat{S}_+^4 + \hat{S}_-^4) - g\mu_B B\hat{S}_n. \tag{B.4}$$

Given the angle of the magnetic field relative to the z-axis of the molecule/crystal, it is then an easy matter to find the eigenvalues of the Hamiltonian and so to know how the allowed energies of the molecule change according to the external magnetic field. A diagram of these energies is shown in Fig. B.1, and the Mathematica code to generate similar diagrams is made available in Appendix E.

Finding the frequency and magnetic field of interaction between the sample and the resonator is now trivial: the energy difference as a function of field strength for the desired transition is calculated from the plot (Fig. B.2a) and compared to the experimentally generated FvB plot for the resonator (Fig. B.2b). The location of interaction is at the intersection (Fig. B.2c).

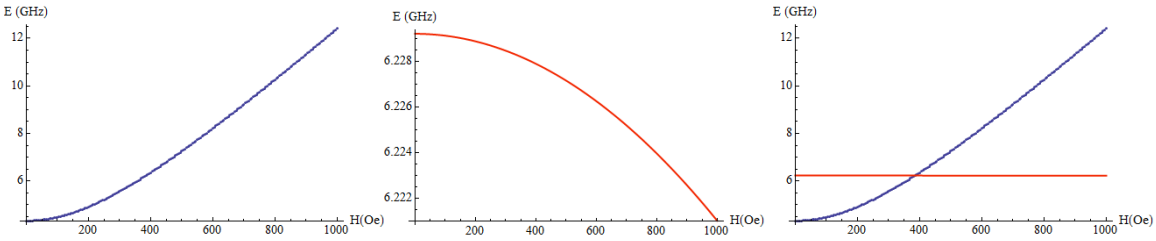

(a) (b) (c)

Figure B.2: Predicted Interaction Field of Sample and Resonator. Where the energy difference between two energy eigenstates (a) matches the resonator's resonance energy (b), we expect to see an interaction (c).

Appendix C

The IQ Mixer and Homodyne Detection[1]

Homodyne detection is central to the operation of the 3G apparatus, since it allows us to extract the phase and magnitude information of the signal that passes through the resonator relative to the known signal originating from the RF generator. Homodyne detection is so called because both the reference signal (or Local Oscillator — LO) and the interesting signal (or just Input Signal — IS) originate from the same source, and so have the same frequency. This is clearly the case for our apparatus, where the two the LO and IS are created by a splitter from the same signal. Homodyne detection thus stands opposite from heterodyne detection, which deals with an LO and IS with different frequencies.

The principles of the IQ mixer are simple. Assume that the LO and IS take the following forms:

$$\begin{aligned} V_{\mathrm{LO}}(t) &= a\cos(\omega t) \\ V_{\mathrm{IS}}(t) &= b\cos(\omega t + \phi), \end{aligned} \tag{C.1}$$

where we see that the IS has identical frequency as the LO, but a distinct amplitude and a phase difference. We can represent each of these signals as polar vectors on the same plane, where the angle between them represents the relative phase difference. For convenience's sake, we fix the LO on the positive x-axis. We would easily be able to extract the IS vector's polar coordinates (which

[1]This section is informed largely by a National Instruments white paper [13], and a short paper by Sabah and Lorenz [22]

are just the magnitude and phase information we are interested in) if we knew its projection onto the x- and y-axes. These projections are effectively the signals that the IQ mixer outputs, conveniently in phase-quadrature, i.e. they are separated by a $\pi/2$ phase shift:[2]

$$\begin{aligned} I(t) &= a * b \cos(\omega t) \cos(\omega t + \phi) \\ &= \frac{a * b}{2} (\cos(\phi) + \cos(2\omega t + \phi)) \\ &= \frac{a * b}{2} \cos\phi \\ Q(t) &= a * b \sin(\omega t) \cos(\omega t + \phi) \\ &= \frac{a * b}{2} (-\cos(\phi) + \cos(2\omega t + \phi)) \\ &= \frac{-a * b}{2} \sin\phi \end{aligned} \tag{C.2}$$

(The double frequency terms average to zero.) These two signals are just orthogonal products of $V_{\mathrm{LO}}(t)$ and $V_{\mathrm{IS}}(t)$. The problem is now purely geometric, and is represented in Fig. C.1. (In the 3G apparatus we obtain the magnitudes of I and Q by measurement with separate lock-in amplifiers.) The interesting information — the phase and magnitude information from IS — is easily constituted with simple trigonometry:

$$\begin{aligned} R = \sqrt{I(t)^2 + Q(t)^2} &= \frac{a * b(t)}{2} \\ \phi = \arctan\frac{Q(t)}{I(t)} & \end{aligned} \tag{C.3}$$

[2]The IQ mixer contains two balanced mixers and two hybrid mixers to achieve this.

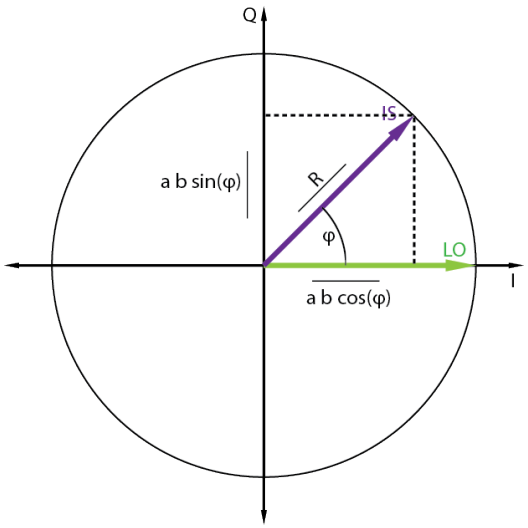

Figure C.1: I and Q output, showing their phase-quadrature relationship.

Appendix D

The Resonator and Circuit Board

As explained in the introduction, we use a resonator as our means of characterizing SMM samples through ESR. To recapitulate, for a resonator with a characterized dependence of its energy eigenvalues upon the applied magnetic field, that field where the behavior of a coupled system deviates appreciably from that of the bare resonator is where there is strong coupling. An analysis of the coupled system's behavior can then determine the relevant energetics of the sample.

Use of a resonator with a high Q-factor is crucial for the above analysis: a low Q-factor can obscure spectroscopic features and render subsequent characterizations imprecise. This consideration has pushed superconducting resonators, such as the superconducting coplanar waveguide (CPWG) resonators that we use, into broad popularity among those practicing ESR.

The specific resonators that we use are part of a series of niobium CPWG resonators manufactured by Saiti Datta in the summer of 2012. A coplanar waveguide resonator consists of two parallel gaps trenched out of a conductor-insulator laminate, as in Fig. D.1. This partitions the conductor, which for us is the Type II superconductor niobium, into two ground planes and one conducting strip or "waveguide". The conducting strip is not a continuous part of the circuit, but rather an island on the insulating substrate that is capacitively coupled to a an RF feedline on either end.

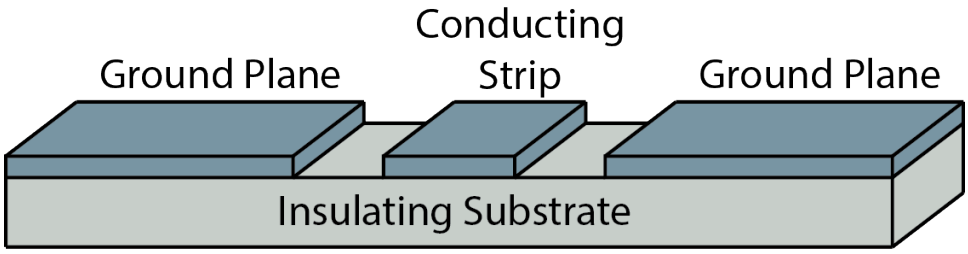

Figure D.1: Coplanar waveguide resonator schematic.

The CPWG resonator supports standing waves according to the equation

$$\nu_n = n\left(\frac{c}{2l\sqrt{\epsilon_{\text{eff}}}}\right) \tag{D.1}$$

where n determines which (first, second, third, etc.) harmonic is being calculated. l is the length of the center conductor, and ϵ_{eff} is the effective dielectric constant.[1] An applied RF signal at one of these frequencies leads to classical resonance behavior, albeit with an extremely high Q-factor if we operate underneath niobium's critical temperature.

Coupling an RF signal through the resonator will cause a magnetic field to oscillate parallel to the plane of the resonator and perpendicular to the conducting strip. A sample of SMMs that is adhered to the surface of the resonator with vacuum grease to conduct the experiment is large compared to the width of the waveguide by at least an order of magnitude, and so to more strongly couple the sample and resonator together we can snake the waveguide back-and-forth underneath the mounted sample. The magnetic fields caused by an oscillating current applied through this back-and-forth pattern (see Fig. D.2) will all be aligned along the longitudinal axis of the circuit board, transverse to the conducting strips. This is convenient given that we want to stimulate the magnetic symmetries of the SMMs, a sample of which can also be aligned along the longitudinal axis.

The resonator is fabricated from niobium to ensure a high Q-factor. Over the span of our research we noted, though, that the niobium resonators degrade over time when exposed to the atmosphere, lowering their Q-factors and thus their usefulness. This process is corroborated by the research of K. Saito, who found that the residual surface resistance of polished niobium can increase by 10nΩ over the course of a week [23]. We found that an effective treatment for restoring degraded Q-factors is to subject the resonator in question to an ultrasound bath in acetone, followed by an ultrasound bath in isopropyl alcohol.

The Circuit Board

The circuit board we use, designed by Adams for his thesis [2] and drawn in Fig. D.2, serves to couple the RF signal from the cabling to the resonator. The connections are simple: the resonator is adhered to the dugout with vacuum grease; its ground plane is connected via aluminum wire bonds

[1] ϵ_{eff} can be experimentally determined by measuring the length of the resonator in question and its resonance frequency; in general the quantity depends on the specific geometry of the resonator and the dielectric constants of surrounding matter [14].

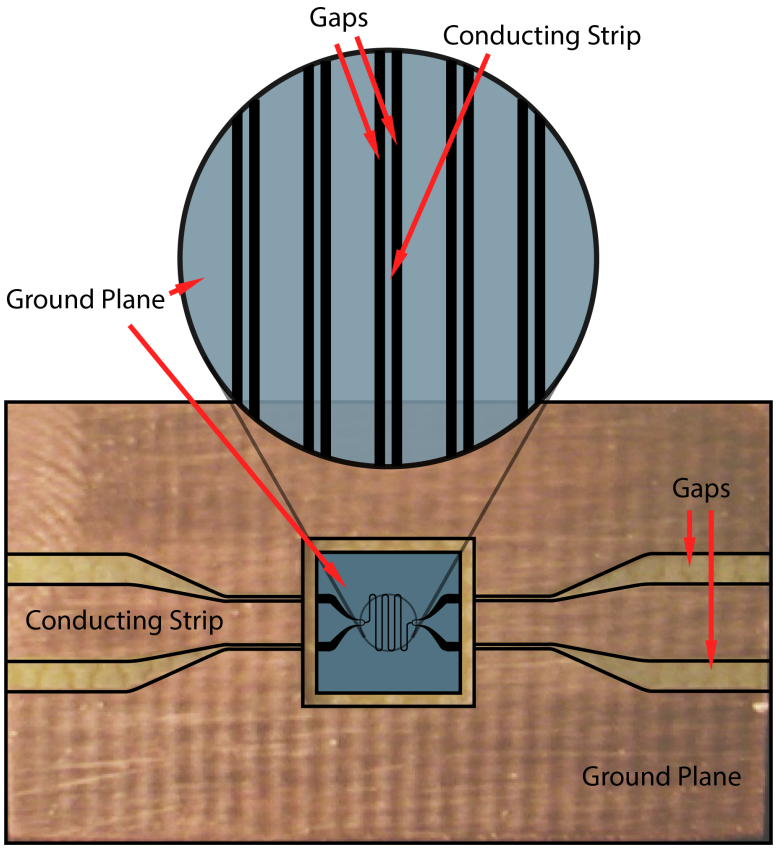

Figure D.2: Circuit board and mounted resonator schematic. Notice that both components are designed as coplanar waveguides, and that their gap and conducting strip dimensions match each other at the interface. (Wire bonds are not shown, but would be densely formed between the conducting strips/waveguides and between the ground planes.)

to the circuit board ground plane, and its conducting strip is connected in the same fashion to the circuit board's conducting strip.[2] The SMA connectors belonging to the coaxial cables carrying the RF signal are mounted to opposite edges of the circuit board as described in Chapter 4 Section 4: the outer conductors are screwed into the circuit board ground plane, and the central conducting pins are secured on pads of soft indium metal.

The board itself is a sandwich: a sheet of ceramic sandwiched between two planes of copper. One face of the copper is milled away in a precision CNC machine to partition the board into a ground plane and a conducting strip (the opposite copper ground plane remains whole). A rectangular dugout is also formed to fit the dimensions of the resonator, such that its surface may sit flush with the copper plane.[3]

The simple design of the circuit board follows from two principles: one, to impedance match the resonators; and two, not to introduce extra sources of parasitic resonances to the circuit, which would complicate measurements. To the first point the peculiar geometry of the circuit board — the ratio of gap width to conducting strip width — is determined by the set of equations from Wadell [27], which are unique to the coplanar circuit board:

$$
\begin{aligned}
z_0 &= \frac{60\pi}{\sqrt{\epsilon_{\text{eff}}}} \left(\frac{k}{k'} + \frac{k_l}{k'_l} \right)^{-1} \\
k &= \frac{\delta}{2\Delta} \\
k' &= \sqrt{1-k^2} \\
k_l &= \frac{\tanh\left(\pi\delta/4h\right)}{\tanh\left(\pi(\delta+2\Delta)/4h\right)} \\
k'_l &= \sqrt{1-k_l^2} \\
\epsilon_{\text{eff}} &= \frac{1+\epsilon_r(k'k_l/kk'_l)}{1+(k'k_l/kk'_l)}
\end{aligned}
\tag{D.2}
$$

Here z_0 is the impedance, δ is the central conductor width, Δ is the gap width (one on each side of the central conductor), h is the board thickness, and ϵ_r is the dielectric constant of the board. If we constrain $z_0 = 50$ Ohms to match that of the resonator, $\delta = .2$ mm to match the central conductor of the resonator, $h = 1.52$ mm and $\epsilon_r = 3.48$ to match our board material,[4] then Δ is uniquely determined to be 1.45 mm.

[2] When forming the bonds between resonator and circuit board, it is desirable to make them as dense as possible; they should approximate a continuous connection interface.

[3] The dimensions of the dugout in the circuit board can be altered to accommodate different resonators without affecting functionality.

[4] The board laminate is Rogers Corporation R04350B with 35μm copper cladding on each side.

To the second point the simplicity of the circuit minimizes extra current paths. An interesting point in the circuit board construction is that the twin copper ground planes, which allows impedance matching with the resonator, also can induce parasitic resonances if the back ground plane is not connected well enough to the front ground plane. On this point we improve somewhat on Adams' design by more thoroughly connecting the planes of copper with the screws that we use to attach the SMA connectors.

Appendix E

Mathematica Scripts

For fitting phase information to an arctangent function

```
initialH = 0;
finalH = 700;
HStep = 5;
outputFolder = "C:\\Documents and Settings\\";
initialFile = "C:\\Documents and Settings\\filename.txt";
filePrefix = StringSplit[initialFile, "H=" <> ToString[initialH]][[1]];
fileSuffix = StringSplit[initialFile, "H=" <> ToString[initialH]][[2]];
exportSuffix = "_Fit Analysis";

Clear[A1, A2, A3, F, Q, a, w];
"Fit is (transmission)=A1+A2*ArcTan[\!\(\*FractionBox[\(2*\((\*\
FractionBox[\(F\), \(2*Q\)])\)*x\), \(\*SuperscriptBox[\(F\), \(2\)] \
- \*SuperscriptBox[\(x\), \(2\)]\)]\)] , taken from p191 of Taylor's \
Classical Mechanics";
"transmission is the measured power, presumably";
"A1 is vertical offset";
"A2 is vertical scale";
"A3 is horizontal scale";
"F is resonance frequency";
"Q is (F/FWHM)";
"x is driving frequency/independent variable";

"creating table to hold data from each test, note that a Peak Voltage \
category has been added";

HLength = (finalH - initialH)/HStep + 1;
dataPoints = Table[0, {HLength + 2}, {12}];
dataPoints[[1]] = {filePrefix, , , , , , , , , , ,};
dataPoints[[2]] = {"Magnetic Field", "A1", "A1-error", "A2",
   "A2-error", "A3", "A3-error", "Central Frequency", "F-error", "Q",
   "Q-error", "R-Squared"};

For[j = 0, j < HLength, j++,
```

```
H = initialH + j*HStep;
HString = "H=" <> ToString[H];

"importing data";
fixedData = Import[filePrefix <> HString <> fileSuffix , "Data"];

"dropping the header from the bits to be analyzed";
fixedData = Drop[fixedData, 1];
"Changing units to MHz from GHz";
fixedData[[All, 1]] = 1000*(fixedData[[All, 1]]);

"Extracting only the frequency and phase data points";
a = {Drop[fixedData[[1]], {2, 4}]};
For[k = 2, k <= Length[fixedData], k++,
 a = Join[a, {Drop[fixedData[[k]], {2, 4}]}]
 ];

"Determining parameter starting values";
GuessA1 = \[Pi]/2;
GuessA2 = 1;
GuessA3 = 1;
GuessQ = 30000;
GuessF = (a[[Position[a, Min[Transpose[a][[2]]][[1]][[1]]][[1]] +
    a[[Position[a, Max[Transpose[a][[2]]][[1]][[1]]][[1]])/2;

"trimming dataset around the peak";
GuessMidIndex = Floor[Length[a]/2];
a = a[[GuessMidIndex - 20 ;; GuessMidIndex + 20, All]];

fit = NonlinearModelFit[a,
  Piecewise[{{A1 + A2*ArcTan[((F)*x)/((F)^2 *(Q) - (Q)*x^2)],
     x < F}, {\[Pi] + A1 +
      A2*ArcTan[((F)*x)/((F)^2 *(Q) - (Q)*x^2)], x > F}}], {{A1,
    GuessA1}, {A2, GuessA2}, {A3, GuessA3}, {Q, GuessQ}, {F,
    GuessF}}, x, MaxIterations -> 1500];

"Fit Values";

"A1";
a1 = fit["BestFitParameters"][[1]][[2]];
a1e = fit["ParameterErrors"][[1]];
"A2";
a2 = fit["BestFitParameters"][[2]][[2]];
a2e = fit["ParameterErrors"][[2]];
"A3";
a3 = fit["BestFitParameters"][[3]][[2]];
a3e = fit["ParameterErrors"][[3]];
"Q";
q = fit["BestFitParameters"][[4]][[2]];
qe = fit["ParameterErrors"][[4]];
"F";
f = fit["BestFitParameters"][[5]][[2]];
fe = fit["ParameterErrors"][[5]];
```

```
  R = fit["AdjustedRSquared"];

  "filling data table";

  dataPoints[[j + 3]][[1]] = H;
  dataPoints[[j + 3]][[2]] = a1;
  dataPoints[[j + 3]][[3]] = a1e;
  dataPoints[[j + 3]][[4]] = a2;
  dataPoints[[j + 3]][[5]] = a2e;
  dataPoints[[j + 3]][[6]] = a3;
  dataPoints[[j + 3]][[7]] = a3e;
  dataPoints[[j + 3]][[8]] = f;
  dataPoints[[j + 3]][[9]] = fe;
  dataPoints[[j + 3]][[10]] = q;
  dataPoints[[j + 3]][[11]] = qe;
  dataPoints[[j + 3]][[12]] = R;

  "printing graph of best fit";

  Print["Fit for " <> HString];
  Print[Show[
    Plot[Piecewise[{{a1 + a2*ArcTan[((f)*x)/((f)^2 *(q) - (q)*x^2)],
        x < f}, {\[Pi] + a1 +
         a2*ArcTan[((f)*x)/((f)^2 *(q) - (q)*x^2)], x > f}}], {x,
      f - 1, f + 1}, PlotRange -> All, PlotStyle -> {Orange}],
    ListPlot[a, PlotRange -> All]]];
  ];

"exporting data table";

Export[outputFolder <> StringSplit[filePrefix, "\\"][[7]] <>
   exportSuffix <> ".csv", dataPoints, "CSV"];
```

For fitting magnitude information to a skewed Lorentzian

```
initialH = 0;
finalH = 1500;
HStep = 20;
outputFolder = "C:\\Documents and Settings\\";
initialFile = "C:\\Documents and Settings\\filename.txt";
filePrefix = StringSplit[initialFile, "H=" <> ToString[initialH]][[1]];
fileSuffix = StringSplit[initialFile, "H=" <> ToString[initialH]][[2]];
exportSuffix = "_Fit Analysis";

Clear[A1, A2, A3, A4, Q, F];
"Fit is (transmission)=A1+A2*(x-F)+\!\(\*FractionBox[\(A3 + A4*\((x - \
F)\)\), \(1 + 4*\*SuperscriptBox[\(Q\), \
\(2\)]*\*SuperscriptBox[\((\*FractionBox[\(x - F\), \(F\)])\), \(2\)]\
\)]\) , taken from Gao's Caltech Thesis, 2008, p.161";
"transmission is the measured power, presumably";
"A1 is vertical offset";
```

```
"A2 is the skew slope";
"A3 is an asymmetry factor. For A3>0, A3<<1 makes quite asymmetrical, \
with the dip on left; as A3->infinity, becomes symmetrical";
"A4 is an asymmetry factor. If positive, dip on left. If negative, \
dip on right. Magnitude affects degree of dip, much like A3. +/-1 \
seem like safe values.";
"Q is resonator quality factor";
"F is central peak Frequency";
"x is independent variable";

"creating table to hold data from each test, note that a Peak Voltage \
category has been added";

HLength = (finalH - initialH)/HStep + 1;
dataPoints = Table[0, {HLength + 2}, {16}];
dataPoints[[1]] = {filePrefix, , , , , , , , , , , , , , ,};
dataPoints[[2]] = {"Magnetic Field", "A1", "A1-error", "A2",
   "A2-error", "A3", "A3-error", "A4", "A4-error", "Q", "Q-error",
   "Central Frequency", "F-error", "R-Squared", "Peak Voltage",
   "Peak Frequency"};


For[j = 0, j < HLength, j++,

  H = initialH + j*HStep;
  HString = "H=" <> ToString[H];

  "importing data";
  fixedData = Import[filePrefix <> HString <> fileSuffix , "Data"];

  "dropping the header from the bits to be analyzed";
  fixedData = Drop[fixedData, 1];
  "inverting curve, and changing units to MHz from GHz";
  fixedData[[All, 2]] = -(fixedData[[All, 2]]);
  fixedData[[All, 1]] = 1000*(fixedData[[All, 1]]);

  "trimming dataset around the peak";
  "GuessA=Max[Transpose[fixedData][[2]]];\[IndentingNewLine]pos = \
Position[fixedData,GuessA][[1]][[1]];\[IndentingNewLine]fixedData = \
fixedData[[pos-300;;pos+100,All]]";

  "Determining parameter starting values";
  GuessA1 = -.0002;
  GuessA2 = 0;
  GuessA3 = 0.0004;
  GuessA4 = -.0009;
  GuessQ = 10000;
  GuessF =
   fixedData[[
     Position[fixedData, Max[Transpose[fixedData][[2]]][[1]][[1]]][[
    1]];
  fit = NonlinearModelFit[fixedData,
    A1 + A2*(x - F) + (A3 + A4*(x - F))/(
     1 + 4*Q^2*((x - F)/F)^2), {{A1, GuessA1}, {A2, GuessA2}, {A3,
```

```
    GuessA3}, {A4, GuessA4}, {Q, GuessQ}, {F, GuessF}}, x,
  MaxIterations -> 1000];


"Fit Values";

"A1";
a1 = fit["BestFitParameters"][[1]][[2]];
a1e = fit["ParameterErrors"][[1]];
"A2";
a2 = fit["BestFitParameters"][[2]][[2]];
a2e = fit["ParameterErrors"][[2]];
"A3";
a3 = fit["BestFitParameters"][[3]][[2]];
a3e = fit["ParameterErrors"][[3]];
"A4";
a4 = fit["BestFitParameters"][[4]][[2]];
a4e = fit["ParameterErrors"][[4]];
"Q";
q = fit["BestFitParameters"][[5]][[2]];
qe = fit["ParameterErrors"][[5]];
"F";
f = fit["BestFitParameters"][[6]][[2]];
fe = fit["ParameterErrors"][[6]];
R = fit["AdjustedRSquared"];

"filling data table";

dataPoints[[j + 3]][[1]] = H;
dataPoints[[j + 3]][[2]] = a1;
dataPoints[[j + 3]][[3]] = a1e;
dataPoints[[j + 3]][[4]] = a2;
dataPoints[[j + 3]][[5]] = a2e;
dataPoints[[j + 3]][[6]] = a3;
dataPoints[[j + 3]][[7]] = a3e;
dataPoints[[j + 3]][[8]] = a4;
dataPoints[[j + 3]][[9]] = a4e;
dataPoints[[j + 3]][[10]] = Abs[q];
dataPoints[[j + 3]][[11]] = qe;
dataPoints[[j + 3]][[12]] = f;
dataPoints[[j + 3]][[13]] = fe;
dataPoints[[j + 3]][[14]] = R;
dataPoints[[j + 3]][[15]] = Max[Transpose[fixedData][[2]]];
dataPoints[[j + 3]][[16]] = Max[Transpose[fixedData][[1]]];



"printing graph of best fit";

Print["Fit for " <> HString];
Print[Show[
  Plot[a1 + a2*(x - f) + (a3 + a4*(x - f))/(
    1 + 4*q^2*((x - f)/f)^2), {x, f - 5, f + 5}, PlotRange -> All,
   PlotStyle -> {Orange}], ListPlot[fixedData, PlotRange -> All]]];
```

```
  ];

"exporting data table";

Export[outputFolder <> StringSplit[filePrefix, "\\"][[7]] <>
   exportSuffix <> ".csv", dataPoints, "CSV"];
```

For predicting interaction location

```
This program calculates eigenstates/energies, magnetization and ESR spectrum
for the S=1 Cr7Mn molecular magnet.  Note that the S=1 model may break down
under certain conditions (high T or high H).

Field is in Oe; Energies are in GHz

Hmin = 0;
Hmax = 2000;
Hstep = 10;

precision = 10;
S = 1;
s = S;
d = 1*21;
d = SetPrecision[d, precision];
e = 1*1.9;
e = 1*SetPrecision[e, precision];
(*The angles theta and phi determine the orientation of the field \
relative to the spin's easy (z) and hard (x) axes.*)
theta = (0 + 0*54.8) Degree // N
theta = SetPrecision[theta, precision];
phi = 0 Degree;
phi = SetPrecision[phi, precision];
g = 2;
\[Mu]b = .001399625;
kb = 20.8366;
hbar = 1;
H1 = 1.;

Deltafunc[i_, j_] := If[i == j, 1, 0];
Sz = Table[i*Deltafunc[i, j], {i, -s, s}, {j, -s, s}];
Sx = 1/2*Table[
    Sqrt[(s - i)*(s + i + 1)]*Deltafunc[j, i + 1] +
     Sqrt[(s + i)*(s - i + 1)]*Deltafunc[j, i - 1], {i, -s,
     s}, {j, -s, s}];
Sy = 1/2/I*
   Table[Sqrt[(s - i)*(s + i + 1)]*Deltafunc[j, i + 1] -
     Sqrt[(s + i)*(s - i + 1)]*Deltafunc[j, i - 1], {i, -s,
     s}, {j, -s, s}];
Splus = Sx + I*Sy;
Sminus = Sx - I*Sy;
(*Sn is the projection of the spin in the direction of the field.*)
Sn = (Sz*Cos[theta] + Sx*Sin[theta]*Cos[phi] + Sy*Sin[theta]*Sin[phi]);
```

```
ematrix = MatrixPower[Sx, 2] - MatrixPower[Sy, 2];

Hamiltonian, eigenvalues and eigenvectors as a function of field along
the direction defined by theta and phi above:

H0[H_] :=
 SetPrecision[-d*Sz^2 + e*(ematrix) - g*(\[Mu]b)*H*Sn, precision]

egsyst = Transpose[Table[Eigensystem[H0[H]], {H, Hmin, Hmax, Hstep}]];

Do[Evalue[H, i] = Chop[egsyst[[1, (H - Hmin)/Hstep + 1, i]]], {H,
   Hmin, Hmax, Hstep}, {i, 1, 2 s + 1}];
Do[Estate[H, i] = Chop[egsyst[[2, (H - Hmin)/Hstep + 1, i]]], {H,
   Hmin, Hmax, Hstep}, {i, 1, 2 s + 1}];

ListPlot[Table[
  Table[{H, (Evalue[H, i])}, {H, Hmin, Hmax, Hstep}], {i, 1,
   2 s + 1}], AxesLabel -> {"H(Oe)", "E (GHz)"},
 AxesOrigin -> {0, -27}]
```

Bibliography

[1] A. Abragam and B. Bleaney. *Electron Paramagnetic Resonance of Transition Ions*. Dover Publications, 1986.

[2] Spencer Adams. Towards an examination of the sweet spot principle in Cr7Mn, a single molecule magnet qubit. Amherst College Senior Honors Thesis, 2013.

[3] Arzhang Ardavan, Olivier Rival, John J. L. Morton, Stephen J. Blundell, Alexei M. Tyryshkin, Grigore A. Timco, and Richard E. P. Winpenny. Will spin-relaxation times in molecular magnets permit quantum information processing? *Phys. Rev. Lett.*, 98:057201, Jan 2007.

[4] Oliver Benson. Aspects of nano-quantum optics. http://www.physik.hu-berlin.de/nano/lehre/Gastvorlesung

[5] D. Bothner, T. Gaber, M. Kemmler, D. Koelle, and R. Kleiner. Improving the performance of superconducting microwave resonators in magnetic fields. *Applied Physics Letters*, 98(10):–, 2011.

[6] D. Bothner, T. Gaber, M. Kemmler, D. Koelle, R. Kleiner, S. Wünsch, and M. Siegel. Magnetic hysteresis effects in superconducting coplanar microwave resonators. *Phys. Rev. B*, 86:014517, Jul 2012.

[7] G. de Loubens, D. A. Garanin, C. C. Beedle, D. N. Hendrickson, and A. D. Kent. Magnetization relaxation in the single-molecule magnet ni 4 under continuous microwave irradiation. *EPL (Europhysics Letters)*, 83(3):37006, 2008.

[8] R. Doll and M. Näbauer. Experimental proof of magnetic flux quantization in a superconducting ring. *Phys. Rev. Lett.*, 7:51–52, Jul 1961.

[9] A.W. Eddins, C.C. Beedle, D.N. Hendrickson, and Jonathan R. Friedman. Collective coupling of a macroscopic number of single-molecule magnets with a microwave cavity mode. *Phys. Rev. Lett.*, 112:120501, Mar 2014.

[10] Jonathan R. Friedman, M. P. Sarachik, J. Tejada, and R. Ziolo. Macroscopic measurement of resonant magnetization tunneling in high-spin molecules. *Phys. Rev. Lett.*, 76:3830–3833, May 1996.

[11] J. Gao, J. Zmuidzinas, B.A. Mazin, P.K. Day, and H.G. Leduc. Experimental study of the kinetic inductance fraction of superconducting coplanar waveguide. *Nuclear Instruments and Methods in Physics Research Section A: Accelerators, Spectrometers, Detectors and Associated Equipment*, 559(2):585 – 587, 2006. Proceedings of the 11th International Workshop on Low Temperature Detectors LTD-11 11th International Workshop on Low Temperature Detectors.

[12] Jiansong Gao. *The Physics of Sueprconducting Microwave Resonators*. PhD thesis, California Institute of Technology, 2008.

[13] National Instruments. What is I/Q data? Technical report, National Instruments, 2014. `http://www.ni.com/white-paper/4805/en/`.

[14] Mark Jenkins, Thomas Hümmer, María José Martínez-Pérez, Juanjo García-Ripoll, David Zueco, and Fernando Luis. Coupling single-molecule magnets to quantum circuits. *New Journal of Physics*, 15(9):095007, 2013.

[15] Vladimir Kresin and Stuart Wolf. *Fundamentals of Superconductivity*. Plenum Press, 1990.

[16] T. Ladd, F. Jelezko, R. Laflamme, Y. Nakamura, C. Monroe, and J. O'Brien. Quantum computers. *Nature*, 464, 2010.

[17] Jonathan Lawrence. *Comprehensive High Frequency Electron Paramagnetic Resonance Studies of Single Molecule Magnets*. PhD thesis, University of Florida, 2007.

[18] Zhengxiang Ma. *RF Properties of High Temperature Superconducting Materials*. PhD thesis, Stanford University, 1995.

[19] Orci. Structure of the single molecular magnet [Mn12O12(O2CC4H3S)16(H2O)4], 2009.

[20] Paul J. Petersan and Steven M. Anlage. Measurement of resonant frequency and quality factor of microwave resonators: Comparison of methods. *Journal of Applied Physics*, 84(6), 1998.

[21] David Pozar. *Microwave Engineering*. John Wiley and Sons, 2001.

[22] S. Sabah and R. Lorenz. Design and calibration of IQ-mixers. In *6th European Particle Accelerator Conference*, 1998. `https://accelconf.web.cern.ch/accelconf/e98/PAPERS/WEP09A.PDF`.

[23] K. Saito. Long term air exposure effect on the electropolished surface of niobium superconducting RF cavity. In *Proceedings of the 1999 Workshop on RF Superconductivity*, 1999.

[24] Howard Snortland. *Nonlinear Surface Impedance in Superconductors*. PhD thesis, Stanford University, 1997.

[25] John Taylor. *Classical Mechanics*. University Science Books, 2005.

[26] Michael Tinkham. *Introduction to Superconductivity*. Dover Publications, 1996.

[27] Brian Wadell. *Transmission Line Design Handbook*. Artech Print on Demand, 1991.

[28] W. Wernsdorfer and R. Sessoli. Quantum phase interference and parity effects in magnetic molecular clusters. *Science*, 284(5411):133–135, 1999.

[29] Anthony Wilson, En-Che Yang, David N. Hendrickson, and Stephen Hill. On the validity of the giant spin approximation and its application to single-molecule magnets. *Polyhedron*, 26(911):2065 – 2068, 2007. Proceedings of the 10th International Conference on Molecule-based Magnets (ICMM 2006) Victoria, B.C., Canada, August 13-17, 2006 {ICMM} 2006.

[30] Xiaobo Zhu, Shiro Saito, Alexander Kemp, Kosuke Kakuyanagi, Shin-ichi Karimoto, Hayato Nakano, William J. Munro, Yasuhiro Tokura, Mark Everitt, Kae Nemoto, Makoto Kasu, Norikazu Mizuochi, and Kouichi Semba. Coherent coupling of a superconducting flux qubit to an electron spin ensemble in diamond. *Nature*, 478, 2011.